Plasmon Hybridization for Enhanced Nonlinear Optical Response

by

Ghazal Hajisalem
BSc., University of Shahid Beheshti, 2005
MSc., University of Shahid Beheshti, 2008

A Thesis Submitted in Partial Fulfillment
of the Requirements for the Degree of

MASTER OF APPLIED SCIENCE

in the Department of Electrical and Computer Engineering

Supervisory Committee

Plasmon Hybridization for Enhanced Nonlinear Optical Response

by

Ghazal Hajisalem
BSc., University of Shahid Beheshti, 2005
MSc., University of Shahid Beheshti, 2008

Supervisory Committee

Dr. Reuven Gordon, (Department of Electrical and Computer Engineering)
Supervisor

Dr. Thomas Darcie, (Department of Electrical and Computer Engineering)
Departmental Member

Abstract

Supervisory Committee

Dr. Reuven Gordon, (Department of Electrical and Computer Engineering)
Supervisor

Dr. Thomas Darcie, (Department of Electrical and Computer Engineering)
Departmental Member

The linear and nonlinear optical response of plasmon hybridized systems is the subject of study of this thesis. Plasmonic silver nanoprisms are able to confine light to a sub-wavelength volume, which provides local field enhancement. This confined field is promising for achieving an enhanced nonlinear optical response. For many of plasmon nanoparticles, however, the plasmonic resonance is not at the near-infrared wavelengths of a Ti:Sapphire laser, the most common source used for ultra-fast measurements. To achieve resonance at these wavelengths, a tuning mechanism is required.

The plasmon hybridization between silver nanoprisms and a thin gold film provides this tuning mechanism, which allows for enhanced optical second harmonic generation. Overlapping the plasmon resonance of the system with excitation source, by varying the spacer layer between the nanoprisms and the gold film, enhances the second harmonic counts by approximately three orders of magnitude. The finite-difference time-domain calculations agree to within a factor of two with the experimental findings in terms of the predicted enhancement factor. This plasmon hybridization approach is promising for future applications, including enhanced multi-photon lithography and nonlinear sensing using metal nanoparticles.

Table of Contents

List of Figures

Acknowledgments

I would like to sincerely thank my supervisor Dr. Reuven Gordon for his guidance and support throughout my Master program. I was fortunate to work under his supervision.

I would like to thank Dr. David W. Steuerman for his support and guidance during my program.

I gratefully thank Dr. Nima Taghavinia and Dr. Maziar Marandi for introducing me to the research in the field of nano optics and for their guidance during my MS program in Physics.

I would also like to convey my appreciation for Dr. Jeff Young of UBC and Dr. Frank van Veggel for their useful inputs and British Columbia Innovation Council for supporting my research.

I gratefully thank Dr. Elaine Humphrey and Adam Schuetze for their valuable guidance throughout the imaging processes. Also, I gratefully thank Jonathan Massey-Allard of UBC for his great SEM images of my samples.

I gratefully acknowledge the critical contributions made by my collaborators throughout this work: Dr. Aftab Ahmed, Dr. Yuanjie Pang, and Ishita Mukherjee.

I acknowledge invaluable discussions with Dr. Hao Jiang, Jamie Morken, and Dr. Jothir M. Pichaandi.

I also gratefully thank Levi Smith and Dr. Aftab Ahmed for their great help in editing of my thesis.

I was lucky to be surrounded by a great group of friends and an excellent team of coworkers and would like to thank them all for their support.

Dedication

To my family.

AND

To Naser Yasrebi

Glossary

List of symbols:

ε_d	Permittivity of dielectric material
ε_m	Frequency dependent permittivity of metal
ε_{mr}	Real part of the frequency dependent permittivity of metal
ε_{mi}	Imaginary part of the frequency dependent permittivity of metal
ω	Angular frequency
ω_p	Plasma frequency
ω_{sp}	Surface plasmon frequency
n	Refractive index
E	Electric field strength
H	Magnetic field strength
k_{spp}	Wavenumber of surface plasmon polariton
σ_{scatt}	Scattering cross-section
σ_{abs}	Absorption cross-section
P(t)	Polarization
E(t)	Electric field strength
χ	Susceptibility
v	Electron velocity field
$\vec{j}$	Current density

ρ	Charge density

Abbreviations:

SP	Surface plasmon
SPP	Surface plasmon polariton
SPR	Surface plasmon resonance
LSP	Localized surface plasmon
LSPR	Localized surface plasmon resonance
LRSP	Long range surface plasmon
SRSP	Short range surface plasmon
TE	Transverse electric
TM	Transverse magnetic
SHG	Second harmonic generation
SEM	Scanning electron microscopy
AFM	Atomic force microscopy
BSE	Backscattered electron
BSPP	Bis (p-sulfonatophenyl) phenylphosphine dehydrate dipotassium salt
PMMA	Poly (methyl methacrylate)
NA	Numerical aperture
ND	Neutral density filter
WLS	White light source
FDTD	Finite-difference time-domain

TFSF	Total field scattered field
PML	Perfectly matched layer
QD	Quantum dot

Chapter 1

1 Introduction

1.1 Thesis Introduction

Plasmonic nanostructures enable confinement of large electromagnetic fields to small volumes. These enhanced local fields are appealing for nonlinear optical processes of metal nanostructures. For example, nonlinear optical response of nanostructures may be incorporated in other media for multi-photon lithography [1].

Many works have studied the second-order optical response of metal nanostructures [2-5]. Of particular interest is second harmonic generation (SHG) of metal nanoparticles. The structural properties of nanoparticles are commonly altered to achieve broken symmetry with greater second harmonic response [6] and the related property of directional enhancement of the nonlinear response [7].

Past works have studied the nonlinear optical response of silver nanoparticles, even mapping down to the single nanoparticle level [8]. Silver nanoprisms are particularly interesting because of their single-crystal structure, the low loss of silver, the sharp tips of the nanoprism, and their asymmetric geometry. Silver nanoprisms smaller than 100 nm do not have a plasmonic resonance at the near-infrared wavelengths of a Ti:Sapphire laser, the most common source for ultra-fast measurements. To achieve resonance at these wavelengths a tuning mechanism is required [9-14]. This mechanism can be achieved by top-down fabrication of multi-resonant optical antenna structures. For particles fabricated by bottom-up methods; such as silver nanoprisms, we propose the plasmon hybridization approach to tune the resonance to that of the laser source.

Plasmon hybridization refers to coupling between metal nanoparticles [15-17], or nanoparticles to other metal nanostructures, such as a metal film, [18-22] in order to tune the optical response. For example, it has been shown that the plasmon resonance of silver nanoparticles can be tuned by various amounts by spacing them off from a gold film with a spacer of various thicknesses [23]. The spacer layer thickness can also be tuned a posteriori by voltage controlled oxidation [24]. Here we are particularly interested in the hybridization between a metal nanoparticle and a thin metal film that supports short-range modes and gives precise tuning of the lowest order resonance [25]. A thin metal

film is advantageous because it can transmit light; for example, in applications where the film is deposited on top of a photoresist layer.

The research described in this thesis addresses the above situation. We use plasmon hybridization between colloidally synthesized silver nanoprisms and a 10 nm thick gold film to tune the plasmon resonance to the peak wavelength of our laser source. At the peak wavelength, we obtain three orders of magnitude enhanced SHG, as compared to the far off-resonance condition of a large spacer layer, or having no metal film at all.

1.2 Authors Contributions

This thesis is based on a project which has been submitted to a scientific journal. The work was carried out by G. Hajisalem, A. Ahmed, Y. Pang, and R. Gordon. The contributions of all authors are provided below:

G. Hajisalem contributed in this project by synthesizing of silver nanoprisms, performing FDTD simulations to design the hybrid systems, fabricating the hybrid systems, performing the linear measurement experiments, performing the second harmonic measurements and contributing to writing a manuscript of article with R. Gordon. A. Ahmed contributed to this project by installing the electronic devices of the synchroscan streak camera, performing FDTD simulations of near-field enhancement and scattering. Y. Pang carried out the FDTD simulations of extinction measurements. All the experiments, FDTD simulations, design of hybrid systems, data analysis and article writing were done under the supervision of R. Gordon.

1.3 Organization of This Thesis

Chapter 2 provides a brief account of the general theory behind surface plasmons and their optical properties. It also reviews plasmonic hybridization, as well as the linear and nonlinear optical responses of plasmonic nanostructures.

Chapter 3 provides short introduction to various pieces of equipment used in this research for characterisation and measurement.

Chapter 4 describes the synthesis method of nanoparticles, the fabrication of hybrid systems, and various characterization methods used in this work.

Chapter 5 describes the linear optical response of the hybrid systems. The experimental setup and measurements details, as well as the simulation details, are provided.

Chapter 6 describes the experiments carries out for the nonlinear optical response of the hybrid systems. Also, near-field simulation details are provided.

Chapter 7 summarizes the work done and outlines possible future directions.

Chapter 8 describes the experimental challenge of using silver nanoprisms synthesized with photo-assist method.

Chapter 2

2 Literature Review

2.1 Introduction

This Chapter provides a brief overview of different types of surface plasmons and their optical properties. Also, it reviews plasmon hybridization to provide a simple, intuitive explanation of the complex plasmonic systems and their properties. Next, it reviews the linear and nonlinear optical responses of plasmonic nanostructures.

2.2 Surface Plasmons

Surface Plasmons (SPs) are collective oscillations of free electrons localized at the interface between a metal (with a large negative permittivity) and a dielectric (with positive dielectric constant). There are two different types of SPs; first, surface waves propagating along the planar interface of metal-dielectric. These waves are known as surface plasmon polaritons (SPPs) [26] (Figure 2-1). Next, localized surface plasmons (LSPs) which are non-propagating surface plasmons, localized on the surface of metal nanoparticles [27, 28] (Figure 2-2). Both SPPs and LSPs are electromagnetic fields localized at the surface of the metal; both of which show significant field enhancement in comparison to the excitation fields. While similar, SPPs and LSPs are not identical; in the two following subsections we briefly summarize SPPs and LSPs, as well as their fundamental features.

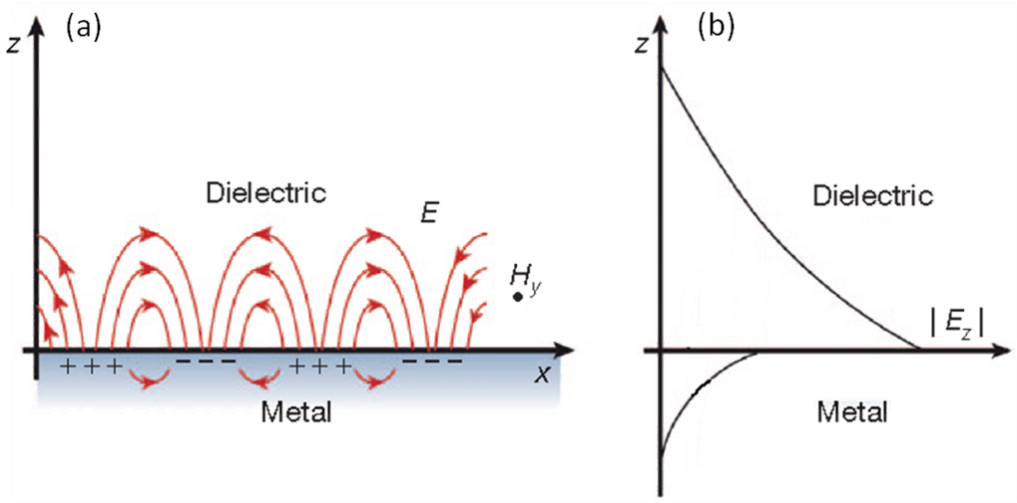

Figure 2-1 (a) An illustration diagram of a SPP (or propagating plasmon). The electric field, E, plotted in the $x-z$ plane and the magnetic field, H_y, sketched in the y direction. (b) An illustration of the SPP electric field decaying in both metal and dielectric media [32]. Reprinted by permission from Nature. Copyright © 2011, Rights Managed by Nature Publishing Group.

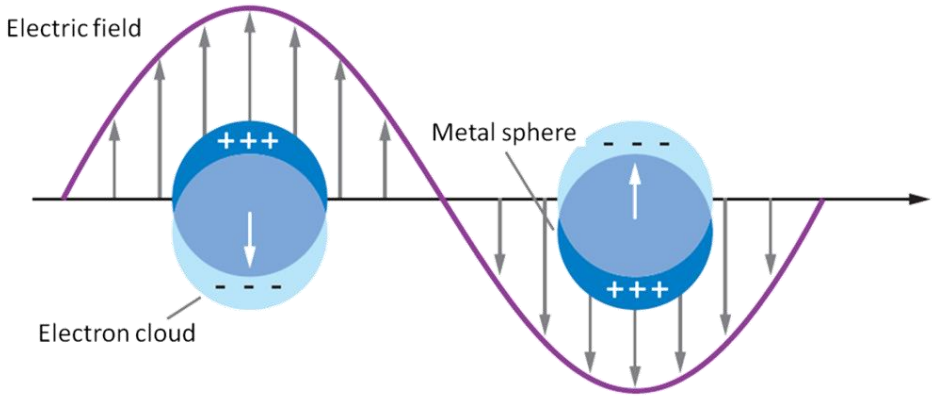

Figure 2-2 An illustration of a LSP [28].

2.2.1 Surface Plasmon Polariton

SPP is specific type of surface wave which is confined at the planar interface of a metal-dielectric [29, 30]. The energy of the wave is shared between electron charge density (plasmon) of the metal and the electromagnetic field. The electromagnetic field decays exponentially along the transverse direction in both the metal and the dielectric

(Figure 2-1). The rate of the decay and mode shape are dependent on the metal, dielectric (insulator), and wavelength of incident light.

We can obtain the dispersion relation and the related field profiles of a SPP on a single metal-dielectric interface by solving the Maxwell's equations and applying the necessary boundary conditions [31].

Here we consider a semi-infinite planar boundary condition in which the $z = 0$ plane is defined as interface between two media in Cartesian coordinates. The dispersion relation along the propagating direction is given as:

$$k_x = k\sqrt{\frac{\varepsilon_m \varepsilon_d}{\varepsilon_m + \varepsilon_d}}. \tag{2.1}$$

Also, wave vectors perpendicular to the interface, *z*-direction, are:

$$k_{m,z} = k\sqrt{\frac{\varepsilon_m^2}{\varepsilon_m + \varepsilon_d}}, \tag{2.2}$$

$$k_{d,z} = k\sqrt{\frac{\varepsilon_d^2}{\varepsilon_m + \varepsilon_d}}, \tag{2.3}$$

where k_x is the wave vector of the SP in direction of propagation, k is the free space wave vector ($k = \omega/c$), ε_m is frequency-dependent permittivity of metal ($\varepsilon_m = \varepsilon_{mr} + i\varepsilon_{mi}$) and ε_d is relative permittivity of dielectric. $k_{m,z}$ and $k_{d,z}$ are the normal components of the transverse wave vector in the metal and the dielectric, respectively.

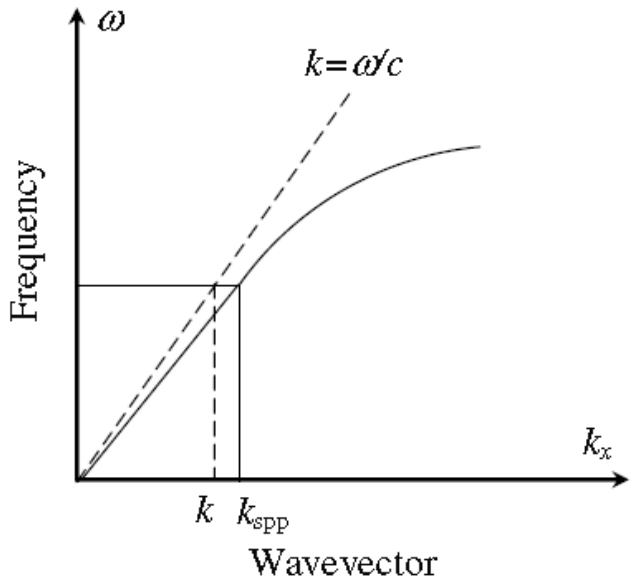

Figure 2-3 Dispersion curve of SPP (solid line) and free space wave vector (dotted line) on a metal surface [32].

It can be seen that the propagation constant k_x tends to infinity as ε_m approaches $-\varepsilon_d$, results in very large imaginary transverse wave vectors. The resulting wave is confined to the surface, decaying exponentially on both sides of the interface (Figure 2-1(b)). Substituting k_{SPP} for k_x , the SPP dispersion relation can be expressed as:

$$k_{SPP} = k \sqrt{\frac{\varepsilon_m \varepsilon_d}{\varepsilon_m + \varepsilon_d}}. \tag{2.4}$$

The momentum of SPP wave ($\hbar k_{SPP}$) is larger than the momentum of light in free space ($\hbar k$) for same frequency (ω) (Figure 2-3). Therefore, to couple the incident light with SPPs and excite the SPP modes, special momentum matching techniques are required, such as prism coupling or grating coupling.

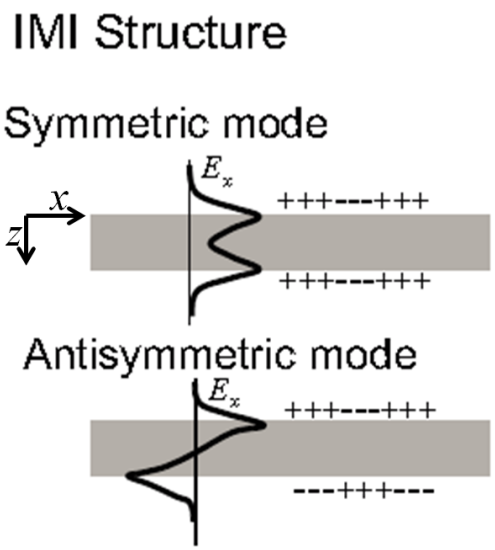

Figure 2-4 Illustrations of symmetric and antisymmetric modes supported by IMI structure. Dark region represents metal film [27].

Insulator-metal-insulator (IMI) and metal-insulator-metal (MIM) structures can also support SPPs, as shown in Figures 2-4 and 2-5. In case of a thin metal film embedded in a dielectric medium, i.e. the IMI case, there are two different SPP waves propagating at the upper and lower interfaces. When the film is thick enough, two SPP modes are separate and independent of each other. But, when the film is thin enough, two SPPs are coupled results in symmetric and asymmetric SPPs modes. The symmetric SPP mode is a result of in-phase superposition of the SPPs at the two interfaces, where the charge distribution is symmetrical. While, the asymmetric SPP mode is consequence of the out-of-phase superposition of the SPP modes, and it has an asymmetric charge distribution.

As the thickness of metal film is reduced, the confinement of the asymmetric modes to the interface is reduced, which forms a long range surface plasmon (LRSP) [33]. In contrast, reducing the thickness of metal film increases the confinement of symmetric modes, and thus the propagation length is drastically reduced. These high attenuation waves are referred to as short range surface plasmons (SRSP).

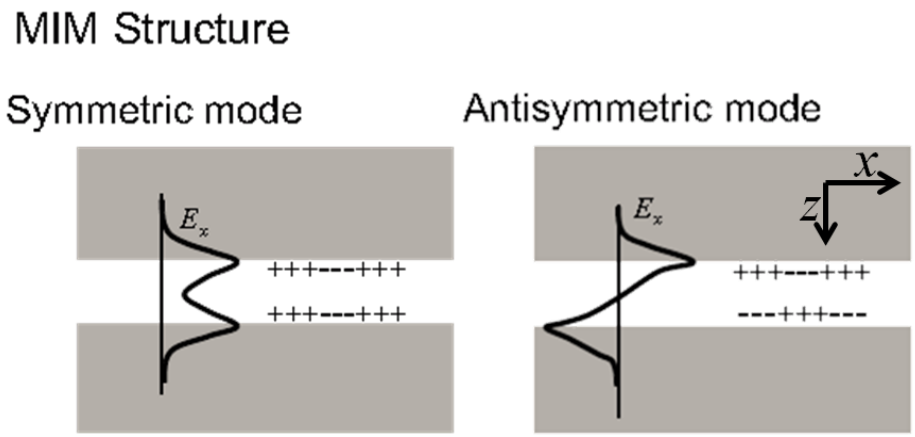

Figure 2-5 Illustrations of symmetric and antisymmetric modes in MIM structures. Dark regions represent metal films [27].

In the metal-insulator-metal structure, a thin insulator (or vacuum) layer is sandwiched between two metals. Figure 2-5 shows symmetric and antisymmetric SPPs in a MIM structure. Interestingly, the lowest order of antisymmetric mode can exist even when the insulator thickness approaches zero. In other words, there is no cut off thickness for this mode [34].

2.2.2 Localized Surface Plasmons

Another type of SPs is the non-propagating SP, which is supported by small metal particles. The electron oscillations are confined by the curved surface of these particles, leading to a resonance (known as localized surface plasmon resonance - LSPR) and consequently a field enhancement both inside and outside of the particle.

The LSPR of metal nanoparticles leads to the colouration of systems containing these nanoparticles. Gustav Mie developed a general electromagnetic theory describing the optical properties of such systems. The Mie theory explains the normal modes and optical response of an arbitrary size sphere [35]. However, in sufficiently small metal particles, the LSP modes can be obtained by applying the simpler quasi-static approach [31]. In this subsection, first we review some results of the Mie theory for spherical particles. Next, using the quasi-static approach, we discuss the electric field inside and outside of very small metal particles and the resulting optical properties of such particles.

Based on the Mie theory, the extinction efficiency Q_{ext} (the sum of the scattering efficiency,Q_{sca}, and the absorption efficiency, Q_{abs}) is calculated in terms of spherical

Bessel and Henkel functions [36]. The extinction efficiency is a function of the sphere's radius, the wavelength of the incident light, and the relative permittivities of involved materials. Particles with positive dielectric constant (e.g. silicon) can support both transverse electric and transverse magnetic (TE and TM, respectively) modes, whereas those with negative dielectric constant (e.g. silver) can only support TM modes [27]. These TM modes are referred to as LSPs.

Figure 2-6 shows spectra of the extinction efficiency of 100 nm silicon and silver spheres surrounded by air. The extinction peaks of silicon particle can be characterized with both TE_l and TM_l modes with $l = 1$ and 2. However, the extinction peaks of a silver particle are attributed to only TM_l modes ($l = 1, 2$ and 3). In the latter case, the extinction peaks correspond to the surface plasmon resonance (SPR) and TM_1, TM_2, and TM_3 are dipolar, quadrupolar, and higher order multipolar LSPs, respectively.

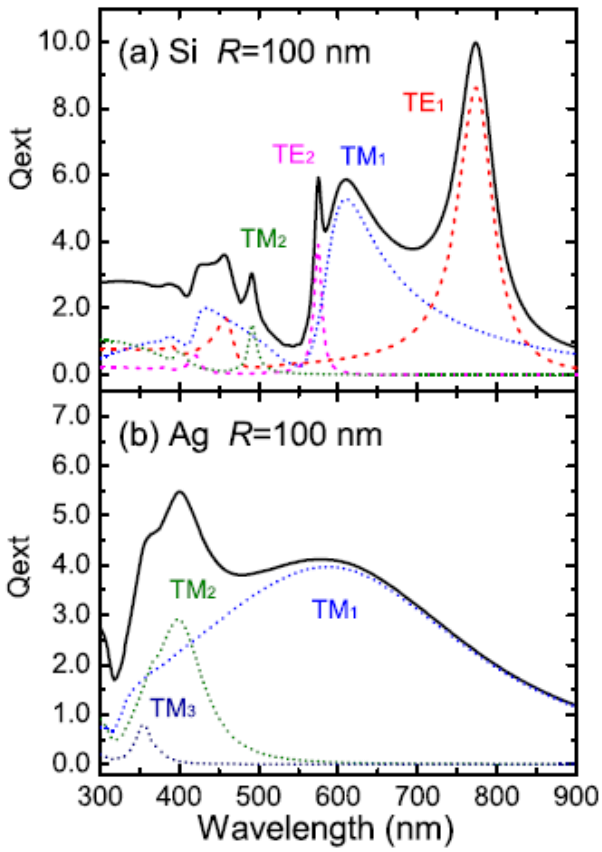

Figure 2-6 (a) Q_{ext} spectrum of 100 nm radius silicon sphere. (b) Q_{ext} spectrum of 100 nm radius silver sphere [27].

Figure 2-7 shows the extinction efficiency spectra of silver spheres with 100 nm, 60 nm, and 20 nm radius. It can be seen that by decreasing the radius, higher order plasmons tend to disappear, such that the 20 nm silver particle supports only the TM_1 mode.

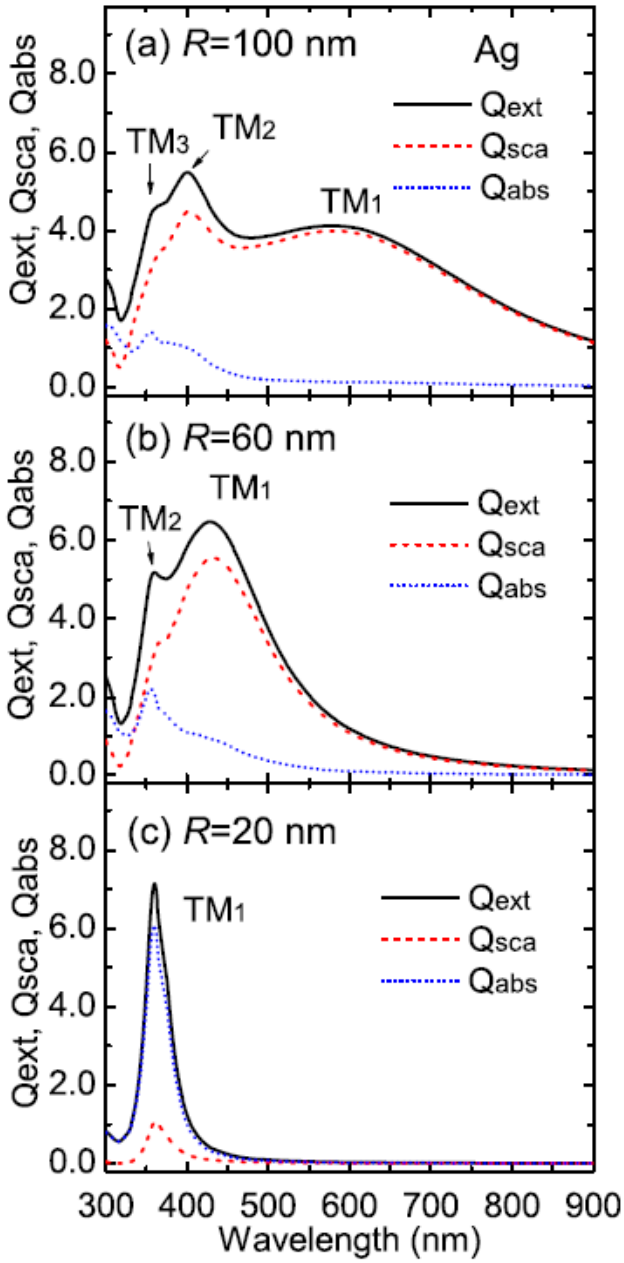

Figure 2-7 Q_{ext} , Q_{sca} , and Q_{abs} spectra of (a) 100 nm radius, (b) 60 nm radius, and (c) 20 nm radius silver spheres. It can be seen that by decreasing the radius, higher order plasmons tend to disappear, such that the 20 nm silver particle supports only TM_1 [27].

While the Mie theory is a rigorous approach to explain the optical properties of spherical particles using classical electromagnetics, a simpler method can be used to approximate the behavior of very small spheres. Here, we use quasi-static approximation by neglecting retardation effects. In the following sections, simple methods such as hybridization, which describe the electromagnetics of interaction between more plasmon structures, are explained.

In the quasi-static approach, it is assumed that all points of the particle respond simultaneously to the excitation (incident) light.

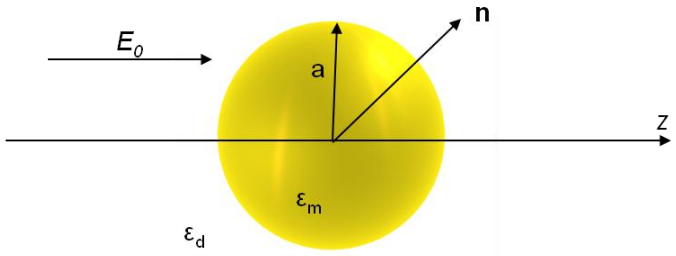

Figure 2-8 An illustration geometry of a metal nanosphere with radius a which is surrounded with a dielectric medium ε_d. Applied external electric field is homogenous, along z-direction and with magnitude of E_0.

Figure 2-8 shows an illustration geometry of a metal nanosphere with radius a, centered at the origin, located in a dielectric medium ε_d. A homogenous electric field along the z-direction, with magnitude of E_0, is applied to the particle. Considering the quasi-static approximation, the Helmholtz equation reduces to the Laplace equation, $\nabla\Phi^2 = 0$, (Φ is the scalar electric potential) . The electric fields are obtained by solving $\mathrm{E} = -\nabla\Phi$.

The electric fields inside and outside of the particle are given as follows:

$$\mathbf{E_{in}} = \frac{3\varepsilon_d}{\varepsilon_m + 2\varepsilon_d}\mathbf{E_0}, \tag{2.5}$$

$$\mathbf{E_{out}} = \mathbf{E_0} + \frac{3\mathbf{n}(\mathbf{n}.\mathbf{p}) - \mathbf{p}}{4\pi\varepsilon_0\varepsilon_d r^3}, \tag{2.6}$$

where r is the radial distance of the observation point from the center of the particle, and $\mathbf{p}$ is the dipole moment given by:

$$\mathbf{p} = 4\pi\varepsilon_0\varepsilon_d a^3 \frac{\varepsilon_m - \varepsilon_d}{\varepsilon_m + 2\varepsilon_d}\mathbf{E_0}. \quad (2.7)$$

From these equations, we can see a resonance occurs for the wavelength where ε_m approaches $-2\varepsilon_d$ [37]. On resonance, the field is strongly localized near the surface of the particle. As a result of applying quasi-static approximation, the electric field inside the metal particle is homogenous.

Figure 2-9 shows the scattering cross-sections of 20 nm silver and gold nanoparticles surrounded by different media. The resonance peaks of the silver nanoparticles are in the ultraviolet spectral range, while gold nanoparticles resonate at around 500 nm. Also, increasing the dielectric constant of the medium shifts the peak position to longer wavelengths.

The removed power from incident light due to the presence of the metal nanoparticles is from both scattering and absorption. The sum of the scattering and the absorption is called the extinction. The scattering-cross section has an a^6 dependence on the radius of the particle, while the absorption cross-section has an a^4 dependence. Therefore, the contribution of scattering and absorption to the net extinction depends on the size of the particles. For large particles, extinction is mainly denoted by scattering, while for sufficiently small particles, absorption is dominant. As a result of this effect, metal particles with different size show different colours. For example, small gold particles absorb green and blue light and render a red colour. While, large gold particles scatter the green light and render greenish colour. Beside the size, the resonance of nanoparticles is dependent on the dielectric constant of their environment (see Figure 2-9).

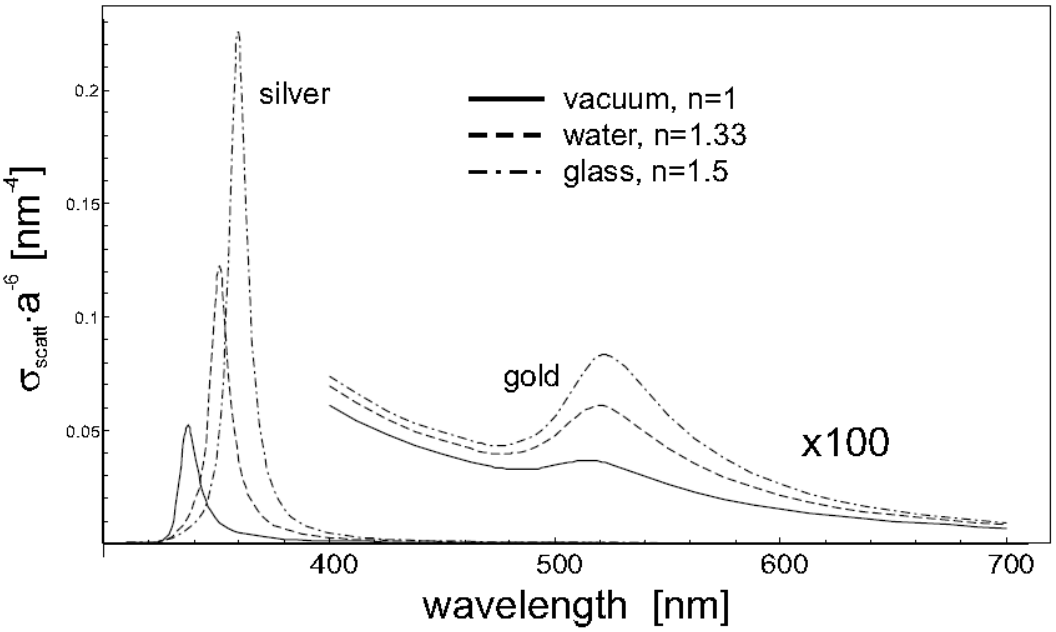

Figure 2-9 Normalized scattering cross-section of 20 nm silver and gold particle in different surrounding mediums. Solid line: vacuum (n=1). Dashed line: water (n=1.33). Dashed-dotted line: glass (n=1.5) [31]. Reprinted with permission.

2.2.3 Effects of Shape and Size on LSP

We can observe LSPR in metal nanoparticles, mostly silver and gold nanoparticles, because they have a plasmon resonance in the visible region of the spectrum. The plasmon resonances of nanoparticles can be tuned to different wavelengths by changing their size and shape, producing different colours [37].

Changing the size of metal nanoparticles shifts their extinction spectra. Figure 2-10 shows scanning electron microscope (SEM) images (left) of gold nanowires with different long axis length and their corresponding extinction spectra (right).

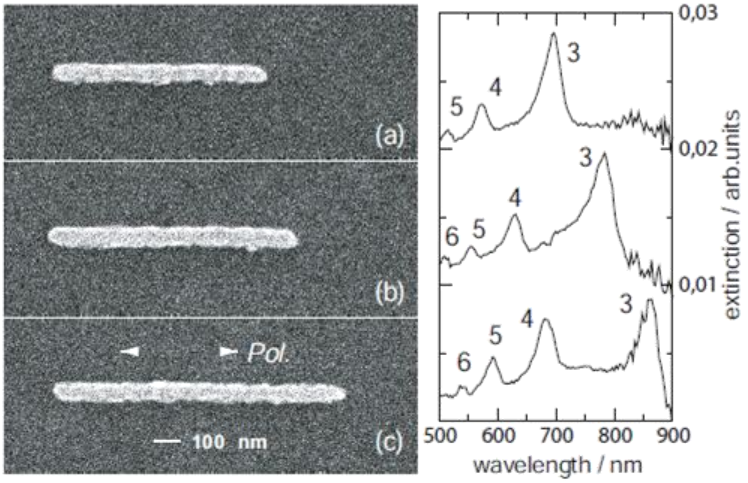

Figure 2-10 SEM images (left) and corresponding extinction spectra (right) of gold nanowires. The exciting light is polarized along the long axis of nanowires. The length of the long axis are (a) 790 nm, (b) 940 nm, and (c) 1090 nm. Numbers at the spectral peaks indicate the order of the multipolar excitation [37].

Figure 2-11 shows the scattering spectra of plasmon nanoparticles with different shapes. It should be noted that the LSPR is strongly dependent on the particle shape.

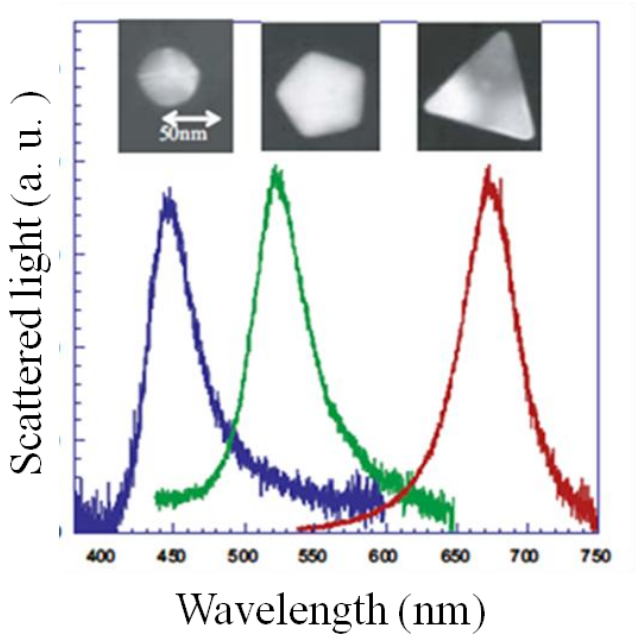

Figure 2-11 Scattering spectra of single silver nanoparticles with different shapes. LSP of nanoparticles strongly depends on their shape [37].

2.3 Hybridization

Simple structures, such as isolated small spheres, show a single resonance peak because of their high symmetry. More complex structures exhibit multi-featured resonance spectra. In addition, they may exhibit strongly enhanced localized field in the gap between particles, known as hot spot, or at the tips of particles. Plasmon resonance of complex structures can be viewed as a result of a hybridization of the elementary plasmons of simpler structures. In this case, the multi-featured plasmon resonance of the structure can be explained by hybridization of the elementary modes. In the following subsections, we explain the interactions between metal nanoparticles forming a more complex system. Next, plasmon modes of some complex structures are described by the hybridization method.

The interaction between metal nanoparticles changes their optical properties. In particular, when gold or silver nanoparticles begin to aggregate, they form pairs of nanoparticles results in colour changing of their solution due to a shift in the plasmon resonance. For example, a diluted solution of gold nanoparticles in presence of ions, e.g. $S_2O_3^{2-}$ ions, can exhibit red-to-blue colour changes. Figure 2-12(a) shows an illustration of isolated gold nanoparticles in comparison to aggregated gold nanoparticles in the presence of $S_2O_3^{2-}$ ions [38]. The corresponding absorption spectra of isolated and aggregated gold nanoparticles as well as SEM images of them are shown in Figures 2-12(b)-(d).

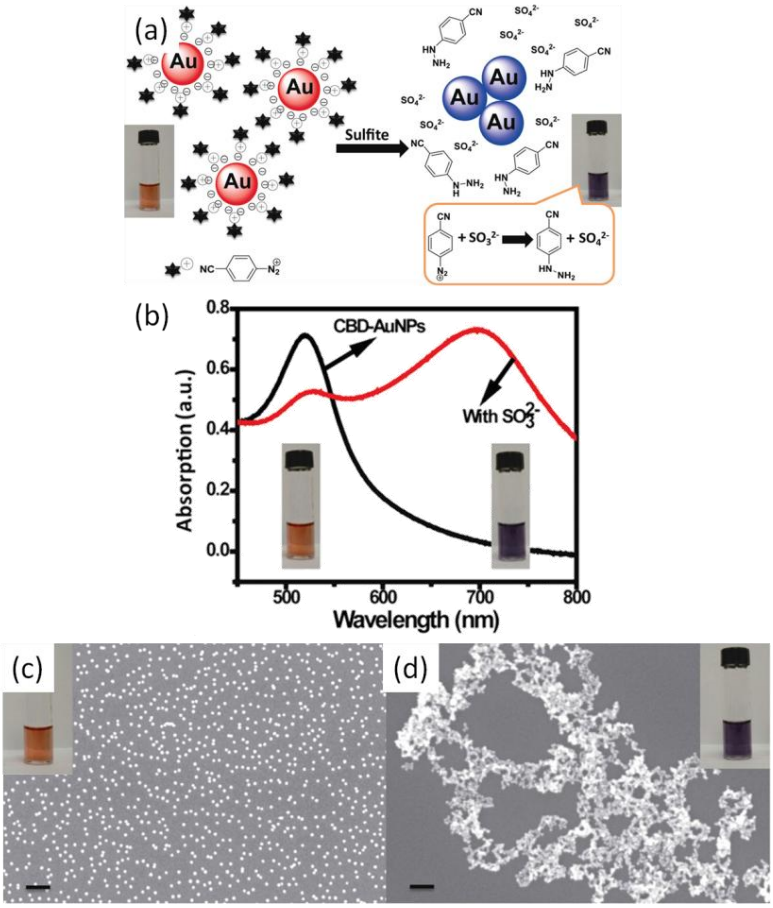

Figure 2-12(a) An illustration of gold nanoparticles (AuNPs) solution, with and without the presence of sulfite ions. Gold nanoparticles were functionalized with 4-cyanobenzene diazonium tetraflouroborate (CBD). (b) Absorption spectra of CBD-AuNPs in the absence and presence of sulfite. (c) and (d) SEM (scale bars: 100 nm) and optical images of CBD-AuNPs in the absence (c) and presence (d) of sulfite. Reprinted with permission from [38]. Copyright © 2012 WILEY-VCH Verlag GmbH & Co. KGaA, Weinheim.

Explaining the field enhancement and the optical response of metal nanoparticles due to their interaction requires an understanding of the electromagnetic properties of interacting metal nanoparticles. For the simplest case, we assume two nearby metal nanoparticles as two nearby oscillators. Their interaction can be explained by coupling of two nearby dipoles. In this case, the interaction energy, V, is proportional to:

$$V \propto {p_1 p_2}/{r^3}\,, \tag{2.8}$$

where p_1 and p_2 are the magnitudes of the dipole moments and r is the interparticle distance. When the nearly adjacent metal nanoparticles are close enough, this interaction

energy is significantly strong, resulting in red-shifted and blue-shifted resonances relative to the resonance of each individual nanoparticles. For the case of two nearby metal nanospheres, the longitudinally aligned dipoles results in a red-shifted resonance. While the transverse coupled dipoles cancel each other, resulting in a zero net dipole moment [39]. Therefore, in this case, the hybrid mode has only one resonance. For more complex systems, the electromagnetic properties are more complicated. However, the hybridization method provides a physical intuitive description for many complex structures such as coupled particles, or asymmetric structures.

2.3.1 Nanoparticle Pairs

Figure 2-13 shows the interaction between a pair of identical metal nanoparticles from hybridization point of view. In this case, different resonance modes may arise depending on the direction of polarization of the excitation light. Therefore, the mutual coupling resonance exhibits red-shift or blue-shift relative to the plasmon of an individual particle depends on the polarization of the excitation light. The red-shifted plasmon mode is referred to as the in-phase plasmon mode or bonding, while the blue-shifted mode is referred to as the out-of-phase plasmon mode (antibonding).

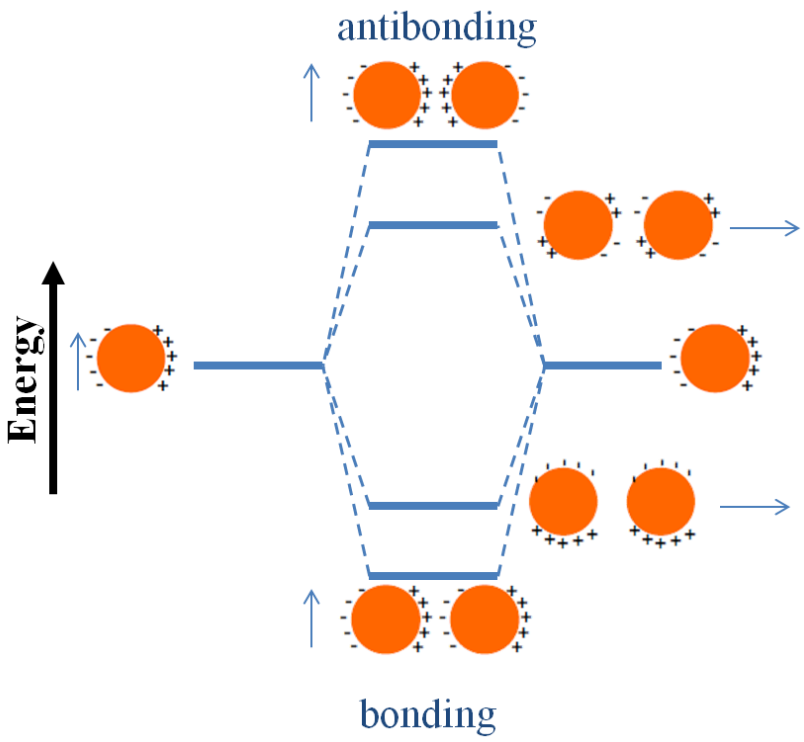

Figure 2-13 Plasmon hybridization in a pair of coupled particles. The blue arrows show the direction of polarization of the excitation light.

2.3.2 Asymmetric Nanostructures

The plasmon hybridization method provides descriptions for single asymmetric particles such as triangular nanowires [31]. Figure 2-14(a) shows near-field distribution of a silver nanowire with triangular cross-section. Here, the direction of the excitation light is shown by white arrows for three different directions. The induced field is sensitively dependent on the excitation direction. Figure 2-14(b) shows the corresponding scattering spectrum of each configuration. The plasmon resonance for excitation in direction 1 is red-shifted in comparison with the plasmon resonance obtained for excitation along direction 2.

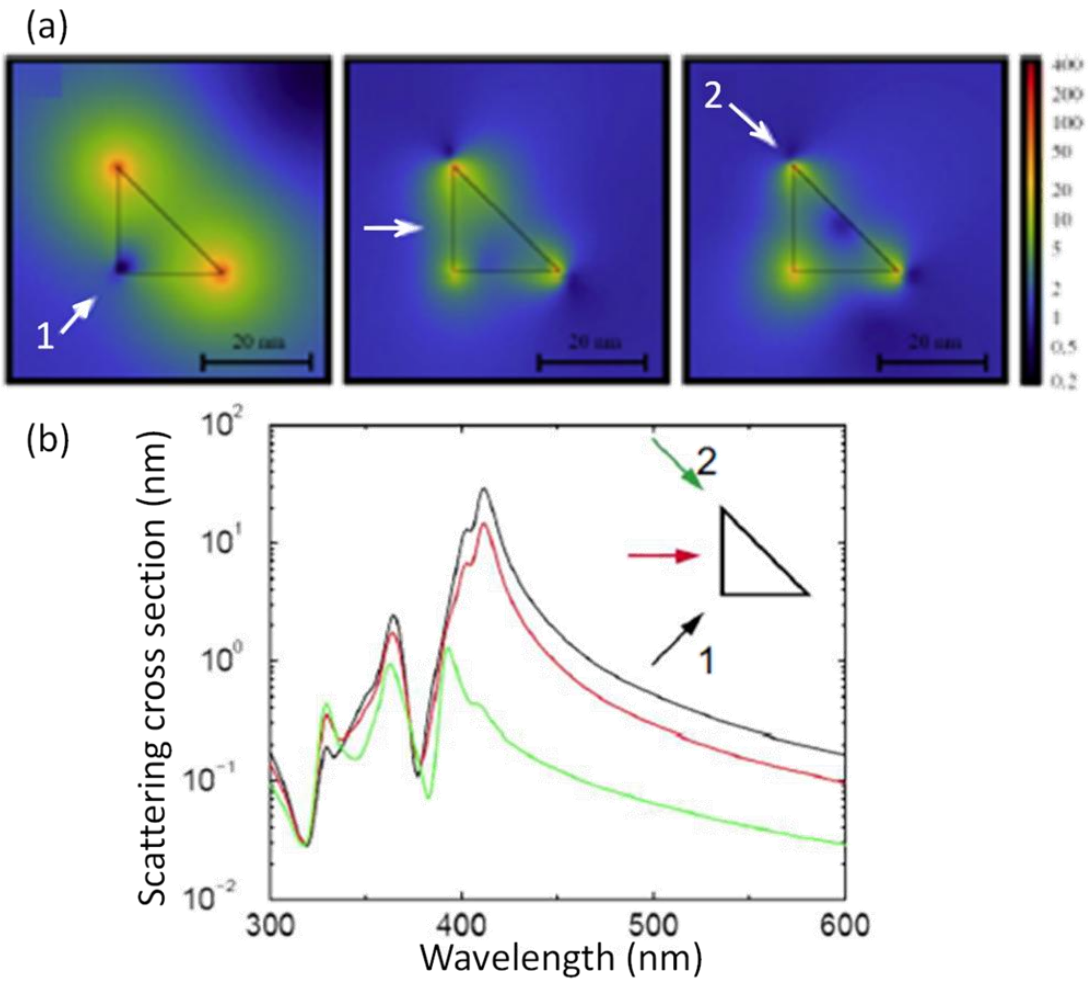

Figure 2-14 (a) Simulated near-field distribution of a silver nanowires for different excitation directions. White arrows indicate the excitation directions. (b) Scattering spectra corresponding to the field distributions shown in (a) [31]. Reprinted with permission.

2.3.3 Thin Metal Films

Coupled plasmon modes of a thin metal film embedded in a dielectric medium can be explained by hybridization method as well. For this structure, the initial plasmon modes are SPP modes propagating freely on top and bottom of the metal-dielectric interfaces. As we discussed in Section (2.1.1), coupling between the upper and lower interface can result in symmetric and antisymmetric plasmon modes based on charge distribution on either side of the film. The lower-energy plasmon corresponds to in-phase superposition , bonding, of individual plasmons, whereas the higher-energy corresponds to out-of-phase superposition of individual plasmons, antibonding. Figure 2-15 shows the plasmon

dispersion of a thin metal film as well as the illustration of charge distribution for in-phase and out-of-phase modes [39]. In the plasmon hybridization picture, the charge distribution on one side of the metal-dielectric interface dictates the charge distribution on the other side of the metal.

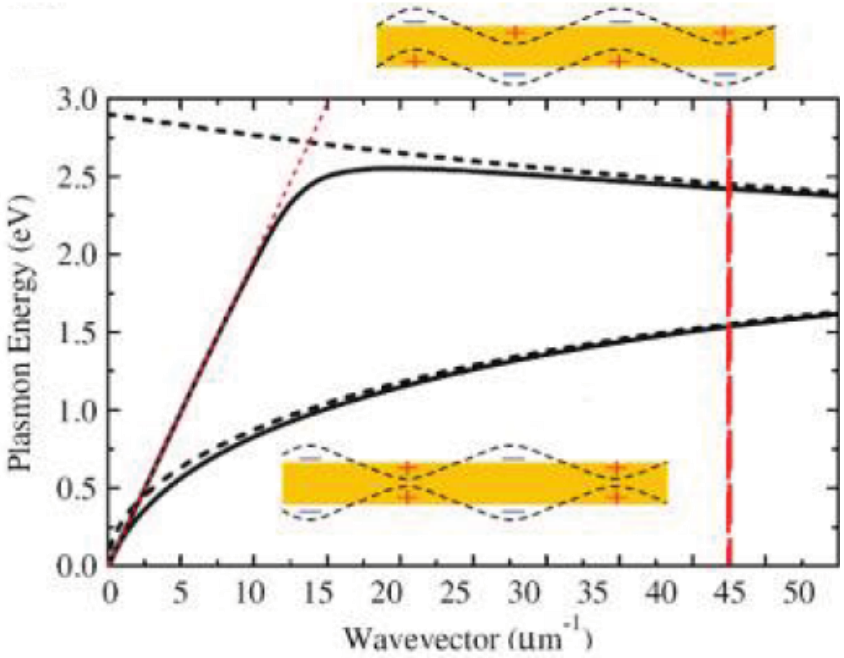

Figure 2-15 In-phase and out-of-phase plasmon dispersion of thin metal film. Bottom inset shows the charge distribution for in-phase plasmon and top inset shows the charge distribution of the out-of-phase plasmon of the film. Reprinted (adapted) with permission from [39]. Copyright © 2011 American Chemical Society.

2.3.4 Nanoparticles over a Surface

Presence of a metal nanoparticle near a substrate breaks the centrosymmetric of the nanoparticle environment. A metal nanoparticle near any substrate results in attraction of the particle to the surface because of the image charges induced in the substrate by presence of particle. This interaction causes a red-shift of the plasmon compared to the plasmon of the individual nanoparticle. For the case of a coupled metal nanoparticle-metal film, in addition to the interaction of particle with its image charges, there is a strong interaction between the LSPs of the nanoparticle and the SPs of the metal film. Hybridization in this system results in either a red-shift or a blue-shift of the plasmon of the nanoparticle, depending on relative energies of the nanoparticle and the SP.

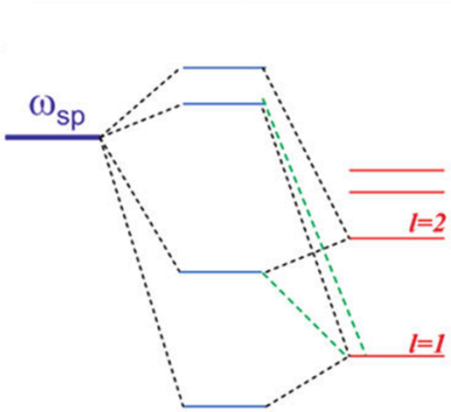

Figure 2-16 The LSPs of metal nanoparticle hybridized with the SPs of metal surface. $l=1$ and $l=2$ are the dipolar and quadrupolar plasmons of nanoparticle, and ω_{sp} is the continuous plasmon of the metal film. Reprinted (adapted) with permission from [39]. Copyright © 2011 American Chemical Society.

Figure 2-16 shows an illustration of hybridization of the LSPs of metal nanoparticle with SPs of the metal film. Discrete LSP modes (*l=1* and *l=2* are the dipolar and quadrupolar plasmons) of the nanoparticle and ω_{sp} is the continuous SP of the metal film. The hybrid plasmon energies strongly depend on the distance between nanoparticle and film, *Z*. Because of the attraction between the particle and its image charges, decreasing *Z* results in reduced energy of the system. Therefore, the resulting plasmon resonance of the coupled system shifts to lower energy relative to the plasmon of the individual nanoparticle. This holds for the case where the SPs of the film are at the same or higher energy than the LSPs of the nanoparticle, e.g. both of them are made of the same plasmon material, such as gold or silver. In case that nanoparticle and film are made of different plasmon materials, decreasing *Z* results in either a blue-shift or red-shift of the hybrid plasmon of nanoparticle. Figure 2-17 shows scattering spectra of a 60 nm diameter silver nanoparticle above a 50 nm gold film for different distances between the nanoparticle and the film. The thin layers of silica with various thicknesses, *d*, were used as spacers. Decreasing the thickness of spacer layer results in red-shift of the plasmon resonance of the system. Insets of Figure 2-17 show dark field images of nanoparticles in each hybrid system as well as an illustration of the hybrid system.

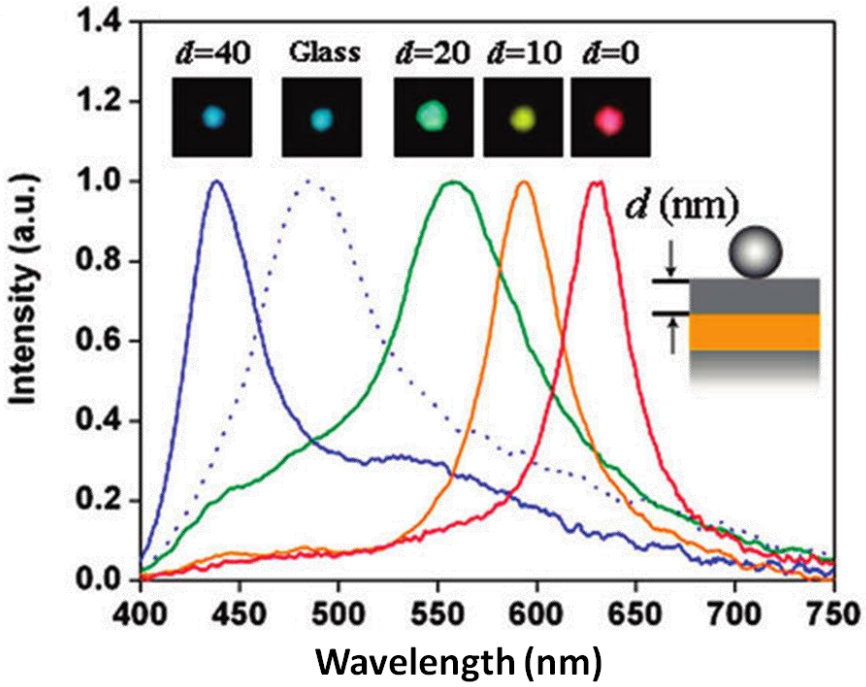

Figure 2-17 Scattering spectra of a 60 nm diameter silver nanoparticle above a 50 nm gold film for different thicknesses, d, of silica as a spacer. Insets show a dark field image of the nanoparticle in each hybrid system as well as an illustration of the hybrid system. Reprinted (adapted) with permission from [39]. Copyright © 2011 American Chemical Society.

Moreover, reducing the thickness of the metal film close to the diameter of the nanoparticle changes the interaction properties of the coupled system. In this case, the hybridized states of the particle-film are changed, depending on the thickness of the metal film. We can describe the interaction model of the particle-film in three following regimes: (1) The image-like interaction which is valid when the thickness of the metal film is much larger than the diameter of the metal particle. (2) The intermediate regime where the thickness of the film is roughly equal with diameter of the particle. (3) A regime where the thickness of film is much smaller than the diameter of nanoparticle. Figure 2-18 depicts three regimes of the interaction between metal nanoparticle and metal film. The plasmonic density of states are shown in light blue, the effective continuum of the film is illustrated in dark blue, and the hybridized plasmons of the system are shown in black.

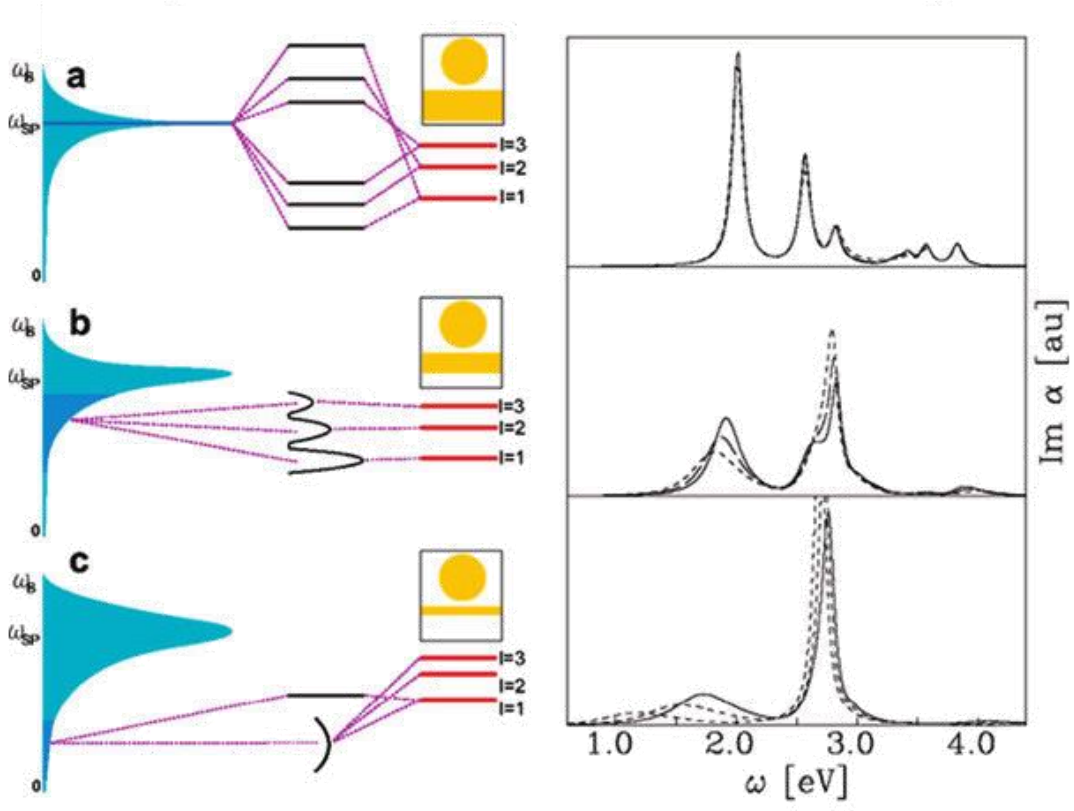

Figure 2-18 The interaction between metal nanoparticle and metal film can be described in three interaction regimes, based on the thickness of the film. (a-c) Three interaction regimes for a plasmonic nanoparticle and SPs of a thin metal film. For each case, the left panel shows the energies of the interaction regime, while the right panel shows the corresponding calculated dipolar optical absorption spectra for various film thicknesses corresponding to this regime. Reprinted (adapted) with permission from [39]. Copyright © 2011 American Chemical Society.

2.4 Second Harmonic Generation

Plasmonics allows for enhanced local electromagnetic fields using metal nanostructures. These enhanced local fields are naturally appealing for nonlinear optical processes. Of particular interest is the second-order nonlinear optical response of metal nanostructures. Second harmonic generation is a second-order nonlinear optical process, where two photons are combined and converted into a single photon with twice the fundamental frequency. SHG is a weak process; therefore, to observe this optical process, the incident light must be of very high intensity, such as those provided by ultrashort pulsed lasers.

Non-centrosymmetry is an important requirement in SHG; therefore, the structure property of a metal nanoparticle is commonly altered to achieve broken symmetry for greater SHG [6].

In this section, we review basic concept of second harmonic generation as well as the correlated linear and nonlinear optical response of plasmon nanostructures.

2.4.1 Introduction to Second Harmonic Generation

Nonlinear optical response of a material is occur when the material system responses to an applied optical field in a nonlinear manner upon to the strength of the electric field. The most common procedure for describing nonlinear optical phenomena is based on expressing the polarization in terms of the applied electric field strength [43]. Here we consider polarization $\tilde{P}(t)$ of a material system depends upon the strength $\tilde{E}(t)$ of the applied electric field. In the case of the linear optics, the induced polarization depends linearly to the electric field strength by the relationship:

$$\tilde{P}(t) = \chi^{(1)}\tilde{E}(t), \tag{2.9}$$

where $\chi^{(1)}$is known as the linear susceptibility. In nonlinear optics, the nonlinear optical response the relation between the polarization $\tilde{P}(t)$ and the field strength $\tilde{E}(t)$ can be described by generalizing the equation (2.9) as a following power series in the field strength as:

$$\tilde{P}(t) = \chi^{(1)}\tilde{E}(t) + \chi^{(2)}\tilde{E}^2(t) + \chi^{(3)}\tilde{E}^3(t) + \cdots \tag{2.10}$$

$$\equiv \tilde{P}(t) + \tilde{P}^{(2)}(t) + \tilde{P}^{(3)}(t) + \cdots. \tag{2.11}$$

The $\chi^{(2)}$ and $\chi^{(3)}$ are the second- and third- order nonlinear optical susceptibilities, respectively. In general, the nonlinear susceptibilities depend on the frequencies of the applied field. But here, for simplicity, the medium is assumed to be lossless and dispersionless, and as a result, the nonlinear susceptibilities are constants. In the equation (2.10), $\tilde{P}^{(2)}(t) = \chi^{(2)}\tilde{E}^2(t)$ refers as the second-order nonlinear polarization, and $\tilde{P}^{(3)}(t) = \chi^{(3)}\tilde{E}^3(t)$ refers as the third-order nonlinear polarization. The second-order interactions are distinct from the third-order optical interactions. Moreover, the second-order interactions can occur only in noncentrosymmetric crystals. For example, in media such as liquids, gases, amorphous solids, and many other crystals with inversion symmetry, the $\chi^{(2)}$ vanished identically, and they cannot produce second-order nonlinear

optical response. On the other hand, the third-order nonlinear optical response can occur both for centrosymmetric and noncentrosymmetric media.

The wave equation in the nonlinear optical media often has the form:

$$\nabla^2\tilde{E} - \frac{n^2}{c^2}\frac{\partial^2\tilde{E}}{\partial t^2} = \frac{4\pi}{c^2}\frac{\partial^2\tilde{P}}{\partial t^2}, \tag{2.12}$$

where n is the refractive index and c is the speed of light in vacuum. In this equation expression, whenever $\partial^2\tilde{P}/\partial t^2$ nonzero, charges are being accelerated, and accelerated charges generate electromagnetic radiation. Therefore, the time-varying polarization can act as the source of new components of the electromagnetic field, and this is the reason of why polarization plays a key role in the explanation of nonlinear optical response.

In the case of second harmonic generation, considering a crystal with nonzero second-order susceptibility $\chi^{(2)}$, the electric field strength of incident light is represented as:

$$\tilde{E}(t) = Ee^{-i\omega t} + c.c., \tag{2.13}$$

where ω is the frequency of the incident light.

Using equation (2.13), the second-order polarization that is created in such crystal is given as:

$$\tilde{P}^{(2)}(t) = 2\chi^{(2)}EE^* + \chi^{(2)}E^2e^{-2i\omega t} + c.c. \tag{2.14}$$

Equation (2.14) shows that the second-order polarization consists of a contribution at zero frequency (the first term) and a contribution at frequency 2ω (the second term). Applying equation (2.12) on equation (2.14), the firs term of equation (2.14) vanishes, while the second term of equation (2.14) can lead to the generation of radiation at the second harmonic frequency.

In case of the SHG at a metal surface, surface plasmons can result in greatly enhanced SHG. In this case, correction terms must be applied to add the contribution terms of surface plasmon [42]. The total charge density ρ and current density $\vec{j}$ satisfy the equation of continuity,

$$\vec{\nabla}\cdot\vec{j} + \dot{\rho} = 0, \tag{2.15}$$

and Euler's equation for the electron fluid,

$$mn\left[\partial\vec{\mathrm{v}}/\partial t + \left(\vec{\mathrm{v}}\cdot\vec{\nabla}\right)\vec{\mathrm{v}}\right] = -en\vec{E} - (en/c)\vec{\mathrm{v}}\times\vec{H} - \overrightarrow{\nabla p}, \tag{2.16}$$

Where m the electron is mass and p is the "quantum pressure",which adds the compression of electrons due to the interactions, $\vec{E}$ is the electric field, $\vec{H}$ is the magnetic

field, and $\vec{v}$ is the electron velocity field. The second-order of optical response of the system is due to the both $(\vec{v}\cdot\vec{\nabla})\vec{v}$ (convection term) and $\vec{v}\times\vec{B}$ (Lorentz term) of equation (2.16). Also, for more complicated systems, such as metal particle nearby a metal film, additional correction terms must ne consider to explain the second-order response of the system.

2.4.2 SHG from Nanoparticles

SHG from nanoparticles strongly depends on the shape of particles as well as the polarization direction of the incident light [40, 41]. Top-down fabrication methods, such as electron beam lithography, can result in homogenous size and shape nanoparticles, and a high degree of the arrangement of particles, but with low crystalline quality. Bottom-up methods, such as colloidal methods, can result in high crystalline quality, easily dispersible nanoparticles, but less control over the size and arrangement of nanoparticles. Here, we review examples of linear and nonlinear optical responses of metal structures fabricated using bottom-up and top-down methods.

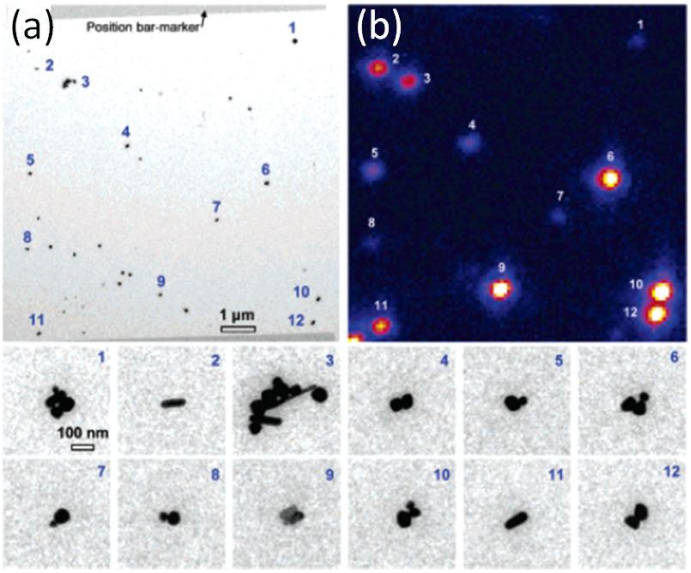

Figure 2-19 (a) Transmission electron microscopy image of silver nanoparticles. (b) SHG map image of the corresponding nanoparticles, excited with 830 nm femtosecond pulses. The bottom panel shows the zoomed-in images of the labeled particles. Reprinted with permission from [8]. Copyright © 2005 American Chemical Society.

SHG in metal nanoparticles depends on the shape of particles, orientation of particles to the polarization direction of the incident light, and interactions between nearby

nanoparticles [8,41-43]. Figure 2-19 shows transmission electron microscope image of colloidally synthesized silver nanoparticles, coated onto a Si_3N_4 substrate and SHG map image of corresponding nanoparticles. The bottom panel shows the zoomed-in images of the labeled particles [8]. A SHG map of the corresponding nanoparticles, at 415 nm when excited with 830 nm pulsed laser, shows the dependence on the shape of particles, as well as the interaction with nearby particles. For example, silver trimer nanostructures (# 6 and 10) and dimers (# 12) can yield high intensity SH signal, based on the shape of particles within the dimer or trimer. The small aggregates (e.g. # 3) may not necessarily generate high SH signal.

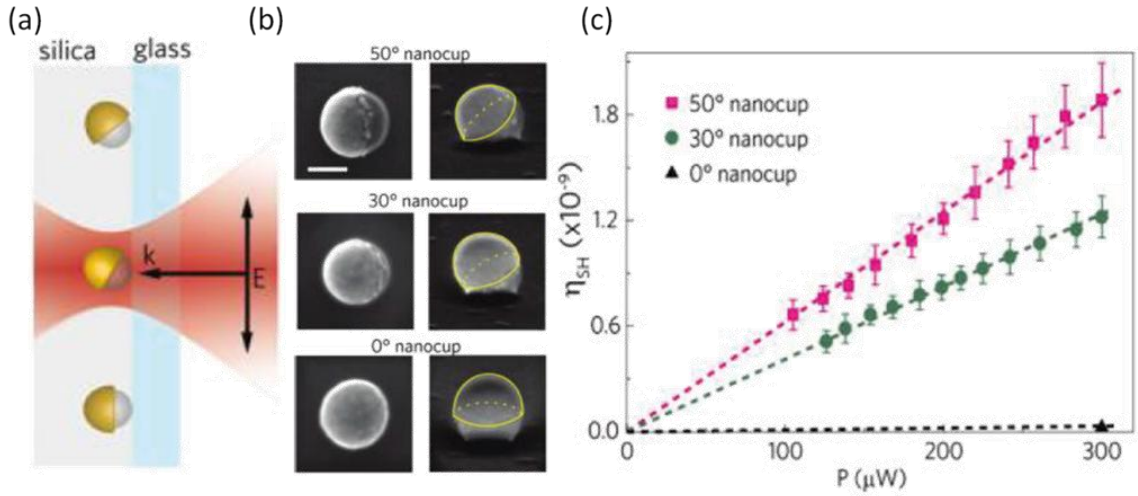

Figure 2-20 Experimental SHG setup of gold nanocup with different orientation to the glass substrate. (a) The illumination geometry of a *p*-polarized incident light (Ti:Sapphire Laser) and a single nanocup. (b) SEM images of gold nanocups oriented at 50°, 30°, and 0° to the normal of the substrate. (c) Corresponding SH conversion efficiency as a function of input power. Reprinted with permission from [7]. Copyright © 2011 American Chemical Society.

In some metal nanostructures, control over emission direction of SHG is possible. For example, in colloidally fabricated metal nanocups deposited on glass substrate, the intensity and direction of SH emission strongly depends on their orientation (Figure 2-20(a)) [7]. Figures 2-20(b) and 2-20(c) show SEM images of gold nanocup oriented at 50˚, 30˚, and 0˚ to the substrate normal and their corresponding conversion efficiency of

SH signal as a function of input power. Increasing the angle between incident light and the symmetry axis of the nanocup results in increasing the intensity of SHG. Moreover, the direction of SH emission of these nanocups depends on their orientation.

SH signal from arrays of metal nanoparticles typically depend on the shape of the nanoparticles, polarization direction of the incident light, linear response of the nanoparticles, crystalline structure, and geometry of the particles.

In bottom-up fabricated gold nanorods, the SH signal sensitively depends on polarization direction of the incident light [41]. Figure 2-21 shows the studied SHG measurement setup as well as dependence of SHG on the excitation power for arrays of gold nanorods. The inset shows a SEM image of the studied nanostructure.

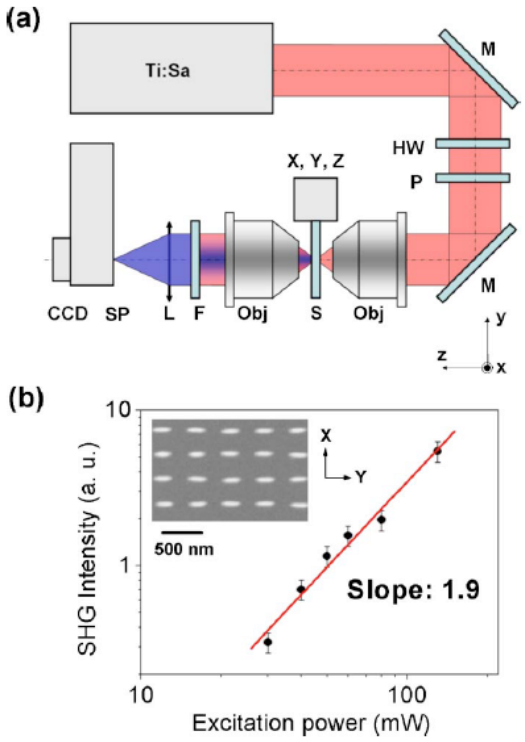

Figure 2-21 Experimental setup of SHG measurement in transmission mode. (b) SHG as a function of excitation power. The LSPR extinction peak was tuned at 800 nm to be matched with a Ti:Sapphire excitation wavelength. The inset shows a SEM image of gold nanorod arrays [41]. Copyright © 2007, American Institute of Physics.

As Figure 2-22 shows, the SHG intensity is maximum when the incident light is polarized along the long axis of the nanorods. Increasing the polarization angle relative to

the long axis of the nanorods decreases the SHG intensity; and at 90˚ polarization angle the SHG is minimum. The LSPR of the nanorods results in a strongly confined energy density. The localized field enhancement boosts the SHG of these nanoparticles.

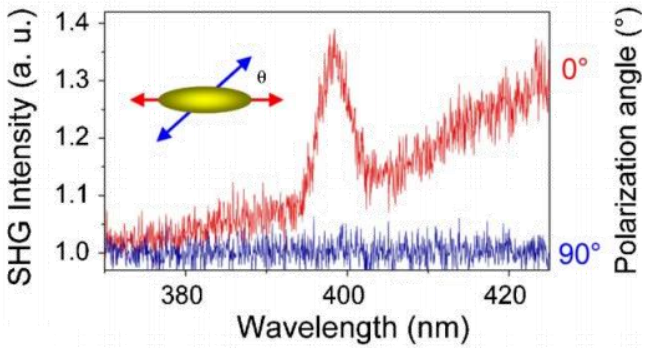

Figure 2-22 SHG intensity of array of gold nanorods at two incident polarization angles [41]. Copyright © 2007, American Institute of Physics.

2.4.3 Relation between Linear and Nonlinear Optical Response of Metal Nanostructures

As we reviewed in the previous sections, plasmonic nanostructures concentrate electromagnetic fields to sub-wavelength regions. This leads to strongly localized field enhancement, which can boost the nonlinear optical response of nanostructures [40, 42]. However, in some cases, the enhanced local fields do not dominantly contribute to the nonlinear properties of the metal nanostructures. In other words, although we expect boosting the nonlinear response of the nanostructures at their hot spots, in some plasmon structures this contribution is negligible. On the other hand, the linear and nonlinear responses of the plasmonic nanostructures are connected [43]. For example, it has been shown that by matching of the linear plasmon resonance of metal nanostructures with the wavelength of excitation source, it is possible to boost the nonlinear response of the nanostructure [44, 45].

As a recently reported example, the third harmonic (TH) response of plasmonic nanoantennas with different geometries, sizes, and shapes have been studied theoretically and experimentally [46]. Third harmonic generation is a nonlinear optical response in which three photons of fundamental frequency are combined to produce a single photon with frequency of three times the fundamental.

In that work, bowtie nanoantennas and triangular nanostructures were excited by femtosecond laser pulses with central wavelength at 817 nm. The nonlinear response of the nanostructures leads to TH emission at 270 nm. Studying the contribution of enhanced local field with TH response properties of these nanostructures has shown that only for nanoantennas with less than 20 nm gap size, the enhanced near-field contributes remarkably to the third harmonic generation signal.

Moreover, the relation between linear responses and TH generation from these structures has been investigated. The extinction spectra of nanoantennas can be tuned between 700 nm to 800 nm by changing the gap size. Figure 2-23 (left column) shows the linear optical response of bowtie antennas with four different gap sizes as well as the incident source peak position (gray spectrum). Figure 2-23 (right column) shows the nonlinear measurements of the corresponding structures. The plasmonic resonance of the bowtie structure is red-shifted into the region of the high intensity of the laser by decreasing the gap size of the bowtie nanoantenna. Simultaneously, as the linear response shifts to the excitation wavelength, the TH signal becomes stronger.

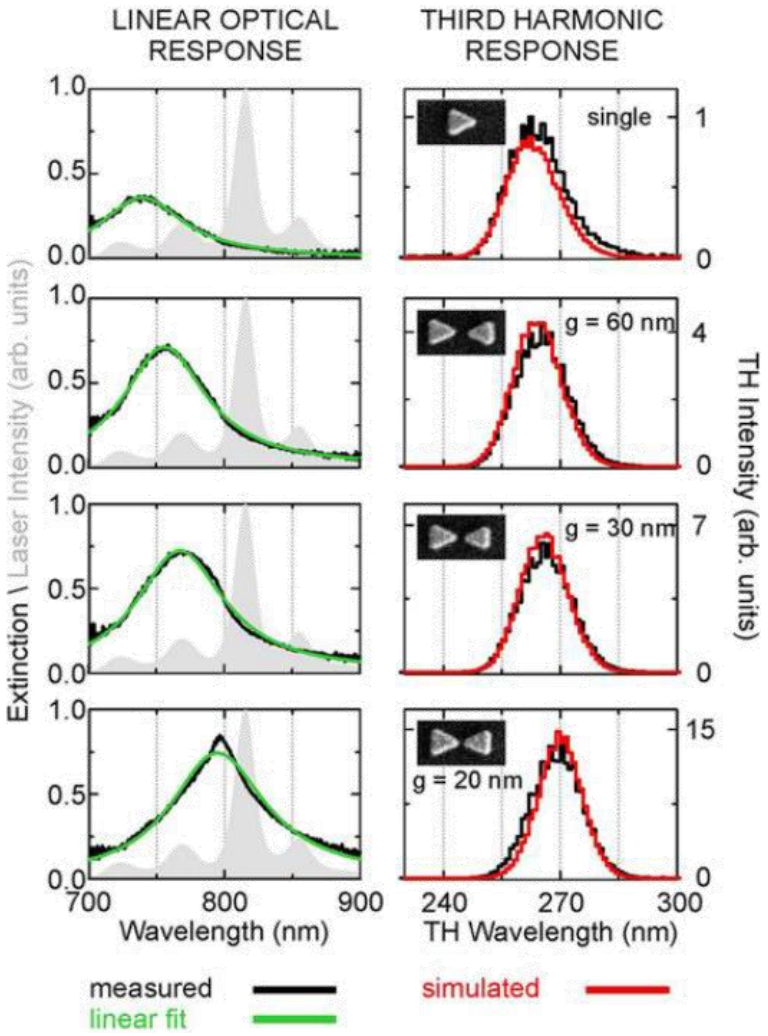

Figure 2-23 Linear (left column) and nonlinear (right column) response of bowtie nanoantennas with different gap sizes. As linear response shifts towards the higher wavelengths and closer to the excitation wavelength, gray spectrum, the nonlinear response increases simultaneously. Insets show SEM images of corresponding nanostructures. Experimental measurements are shown with back line. Simulation results of TH signal are shown with red lines. Green spectrum is linear fit of linear measurements. Reprinted with permission from [46] © 2012 American Chemical Society.

2.5 Silver Nanoprisms

In this project, we have used silver nanoprisms as the plasmon nanoparticles to generate SH signal. The low loss of silver makes it an interesting plasmonic material for weak processes such as SHG. The particles were synthesized in a photo-assisted colloidal

method [47-52], which results in silver nanoprisms with high crystalline quality and a highly homogenous size distribution. Lack of inversion symmetry and the sharp tips are important features of nanoprisms in enhancing of the SHG process.

2.6 Summary

This Chapter started with a brief review on the concept of SPs. Next, the hybridized plasmon systems were explained. Then, linear and nonlinear optical responses of metal nanostructures were discussed. Last, features of silver nanoprisms as plasmon nanoparticles were explained.

Chapter 3

3 Equipment

3.1 Introduction

This Chapter provides an overview of the equipment used throughout my research.

3.2 Scanning Electron Microscope

A scanning electron microscope (SEM) is an instrument that renders an image of nanometre scale objects. The image is produced by raster scanning a high-energy beam of electrons and measuring the signal generated by the electron interaction with the surface atoms. This signal contains valuable information about the morphology, topography, composition, and crystallographic of the surface of the sample [53].

In this project, a Hitachi S-4800 SEM has been used for imaging the metal nanoparticles described in Chapter 4.

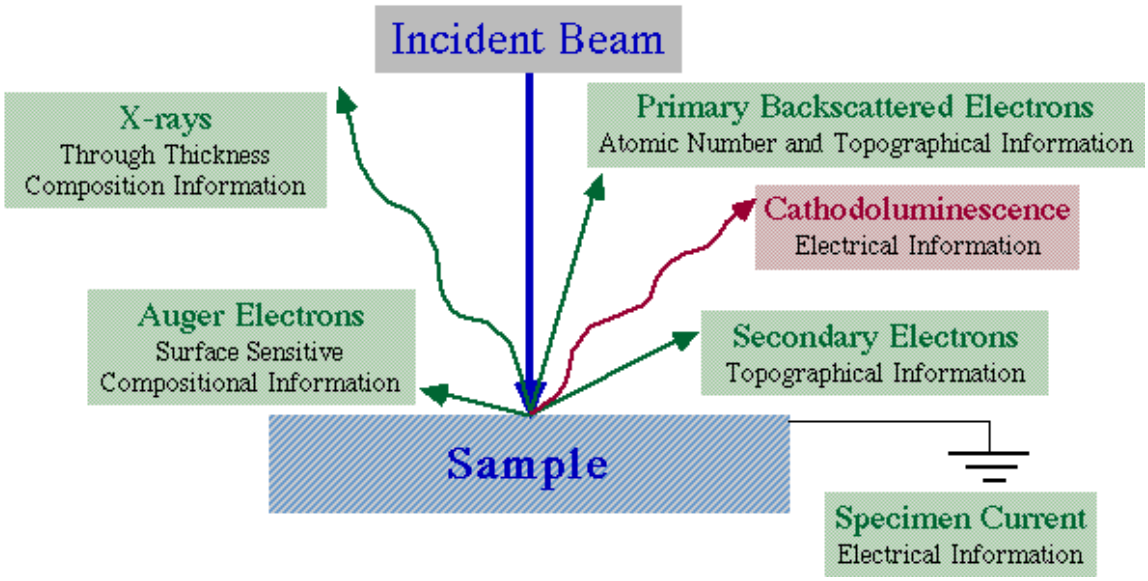

Figure 3-1 Interaction of electron beam with the sample generates both electron and photon signals [54].

3.2.1 Interaction between Electron Beam and Sample

Interaction of the electron beam with the atoms of the sample generates both electron and photon signals. Three types of generated signals commonly used are the secondary electrons, backscattered electrons, and x-rays. Figure 3-1 shows different types of information (signals) that can be gathered from a sample under SEM observation.

Secondary electrons: Secondary electrons are sample electrons that obtain energy by inelastic collisions with beam electrons. They are defined as electrons emitted from the sample with energy less than 50 eV. Secondary electrons are predominantly produced by the interactions between energetic beam electrons and weakly bonded conduction-band electrons in metals or the valence electrons of insulators and semiconductors. There is a significant difference between the amounts of energy contained by beam electrons compared to the sample electrons; therefore, only a small amount of kinetic energy can be transferred to the secondary electrons. The SEM uses an electron detector to convert the radiation of interest into an electrical signal which can be used for imaging.

Backscattered Electrons: Backscattered electrons (BSE) consist of high-energy electrons originating in the electron beam, which are reflected or back-scattered out of the sample interaction volume by elastic scattering interactions with sample atoms. The BSE are used to detect contrast between areas with different chemical compositions, since heavy elements (high atomic number) backscatter electrons more than light elements (low atomic number), and thus appear brighter in the image.

X-rays: In an SEM, x-rays are produced by accelerating the primary electron beam with enough current to pass through the sample thereby interacting with the elements inner core electrons. The release of energy from the escaping electrons from the inner most orbiting shell or (core electrons) is analyzed. Characteristic x-ray radiation allows for microanalysis and distribution of elements of a given sample.

3.3 UV-VIS-NIR Spectrometer

In this research, we have used a Cary 5 UV-VIS-NIR spectrometer to monitor the extinction of colloidal samples as a function of time (Figure 3-2(a)). Figure 3-2(b) illustrates the light path inside a typical spectrometer. In general, a white light source (WLS) is directed to a dispersive device, such as a prism and holographic grating, after which the various wavelengths of light are dispersed at different angles. For clarity, the combination of the entrance slit, dispersive device, and exit slit are referred to as the monochromator. After passing though the monochromator, light exits as a band to be passed through the sample of interest, and finally goes to the detector. The absorbance spectrum can be evaluated by comparing the intensity of the light which passed through the sample with the intensity of the light which passed through a reference. In our case,

the solvent of the samples is de-ionized (DI) water; therefore, DI water was used as the reference in this project. The difference between the samples absorption spectrum and the reference spectrum results in the extinction spectrum of each sample.

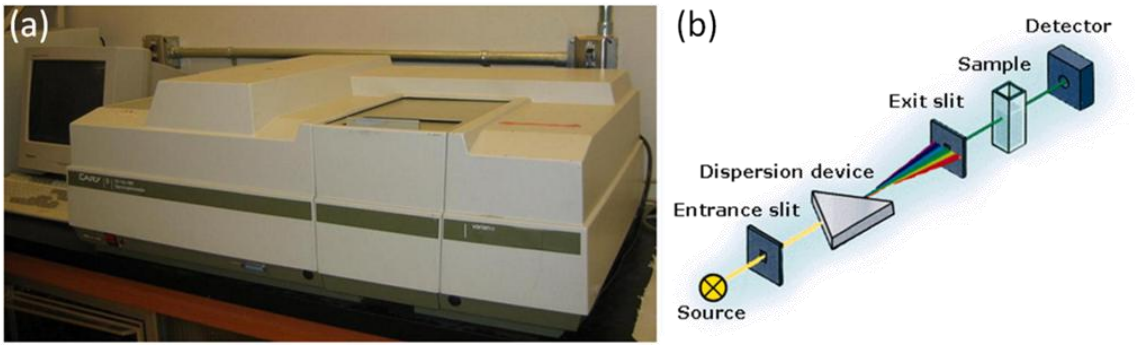

Figure 3-2 (a) Cary 5 UV-VIS-NIR spectrometer. (b) An illustration of light path inside a typical spectrometer, from the white light source to the detector.

3.4 Ti:Sapphire Laser

A laser is an optical oscillator which generates a coherent beam of light at a precise wavelength. All lasers include a few main components: a gain medium, pump, high reflector, and output coupler. This section gives a brief description of these components [55].

Gain medium (also called lasing medium): The gain medium generates optical gain from the stimulated emission during electronic transitions. When the light passes through the gain medium, it is intensified or amplified. Certain crystals, typically doped with rare-earth ions, e.g. neodymium, ytterbium, or erbium, or transition metal ions, e.g. titanium or chromium, and also yttrium aluminium garnet YAG, yttrium orthovanadate YVO_4, and sapphire Al_2O_3, are some examples of gain media.

In order to lase, the atoms in the gain medium must be "prepared" to be in a nonthermal energy distribution, which is known as population inversion. The preparation of this state requires an external energy source known as laser pumping.

Energy (pump) source: Pump is an external source transferring energy to the gain medium of the laser. Absorbing the pumped energy in the medium excites states in its electrons. When the number of particles in one excited state exceeds the number of

particles in the ground state or a lower-energy state, population inversion is achieved. In this condition, the gain medium is prepared for stimulated emission. The power of the pump must be higher than the lasing threshold of the laser. In the case of external optical pumping, a suitable laser can be used to pump another laser. Argon-ion lasers, emitting at 514.5 nm, and frequency-doubled Nd:YAG, Nd:YLF, and Nd:YVO lasers, emitting at a wavelength between 527 nm to 532 nm, are some examples of external optical pump lasers.

Laser cavity: The region of space between the high reflector and the output coupler is referred to as the laser cavity.

High reflector and output coupler (or partial reflector): Light passing through the prepared gain medium are intensified or amplified. The light reflector at one end of the laser, and the output coupler, at the other side, are aligned to return the amplified light towards the gain medium for further amplification. The light passes many times through the gain medium in this rotation. The light travels strictly perpendicular to the reflector and output coupler in a precise direction. Therefore, the generated beam is significantly amplified and highly directed. The output coupler provides the output of the laser. It reflects most of the incident light but allows a fraction to be transmitted, forming the output beam.

3.4.1 General Features of Ti:Sapphire Laser

The titanium:Sapphire laser, also known as Ti:Sapphire laser or Ti:Al_2O_3 laser, is a tunable laser that can generate femtosecond pulses. These two features have made Ti:Sapphire of particular interest for nonlinear optical applications. The emitted light of laser is tunable in the range from 650 nm to 1100 nm; however, it operates most efficiently at around 800 nm [55].

The name of Ti:Sapphire refers to its gain medium, a crystal of sapphire (Al_2O_3) which is doped with titanium ions. Usually a Ti:Sapphire laser is pumped with the output of a continuous-wave laser, which operates in a wavelength between 514 nm to 532 nm.

Ti:Sapphire lasers can output a continuous-wave or ultrashort pulses. In continuous-wave mode, Ti:Sapphire can be tuned over a wide wavelength range with extremely narrow line widths. However, the main applications of the laser are in ultrashort pulses using the mode-locking technique.

Within the cavity of a mode-locking laser, a signal of a short pulse of light bounces back and forth between mirrors. At each bounce from the output coupler, a small fraction of the pulse transmits to form the output of the laser. The time interval between the pulses is equal to the time it takes for light to make one circle path from the output coupler to the high reflector and back to the output coupler; the inverse of this time interval is referred to as the repetition rate. For example, the Ti:Sapphire laser used in this research (KMLabs, Chinook Ti:Sapphire Laser Oscillator) has a repetition rate of 90 MHz.

3.5 Streak Camera

The streak camera is an instrument used to measure ultra-fast light phenomena, and the output images of camera contain intensity vs. time vs. position information of the incident (input) light. In other words, it can measure the light intensity simultaneously on both the temporal and spatial axis. In addition, the camera can detect and measure very faint input light on the order of a few photons. Because of these features, the streak camera has applications in many research fields such as nanophotonics (e.g. SHG measurement), semiconductor physics (e.g. photoluminescence time-resolved spectroscopy of GaAlAs), photochemistry (e.g. picoseconds time resolved absorption of photochromic compound), optical communication (e.g. time-resolved chromatic dispersion measurement in single mode optical fiber), laser-induced discharge measurement, high energy laser nuclear fusion (e.g. measurement of the intensity and the response time of light produced through the reactions). In the following subsections, we review the operation principles of a streak camera, and specific features of the C5680 Hamamatsu streak camera which was used in this research. We also discuss the photon counting principles, and setup alignment steps for photon counting measurement in this research.

3.5.1 Operating Principle

Figure 3-3 shows the process of imaging in a streak camera for four incident light pulses [56]. To measure the light pulse, it is projected onto the slit of the streak camera. The optical image is focused on a photocathode of the streak camera by a lens. In the photocathode, the incident light pulses (photons) are converted into electrons (photoelectrons). The number of generated photoelectrons is proportional to the intensity

of the incident light. The four light pulses are converted in sequence to groups of electrons, and then they are accelerated and sent through high-speed sweeps. A high voltage is applied to electrons while they are passing between a pair of vertical sweep electrodes, and electrons are swept in the direction from top to bottom. Therefore, electron groups which are passing the sweep electrodes at different times are deflected from top to bottom. At the same time, a high-speed and high voltage sweep can be applied on electrons in horizontal direction which deflects the electrons at slightly different positions in the horizontal direction. The swept electrons are directed to the micro-channel plate (MCP). When the electrons pass the MCP, they are multiplied several thousands of times (based on adjustment of the MCP). These electrons then bombard the phosphor screen, where they are converted back into photons.

The optical image which is produced on the phosphor screen is called the "streak image". The vertical axis direction of the image on the phosphor screen serves as temporal axis. For example, the fluorescence image corresponding to the first incident pulse is positioned at the top of the screen, and the last incident pulse is positioned at the bottom of the screen. The spatial information is output to the horizontal axis direction of the phosphor screen. In addition, the brightness of fluorescence image is proportional to the intensity of the corresponding incident light pulse. Therefore, one single streak image contains information about temporal, spatial, and light intensity (number of photons) of the incident light [57].

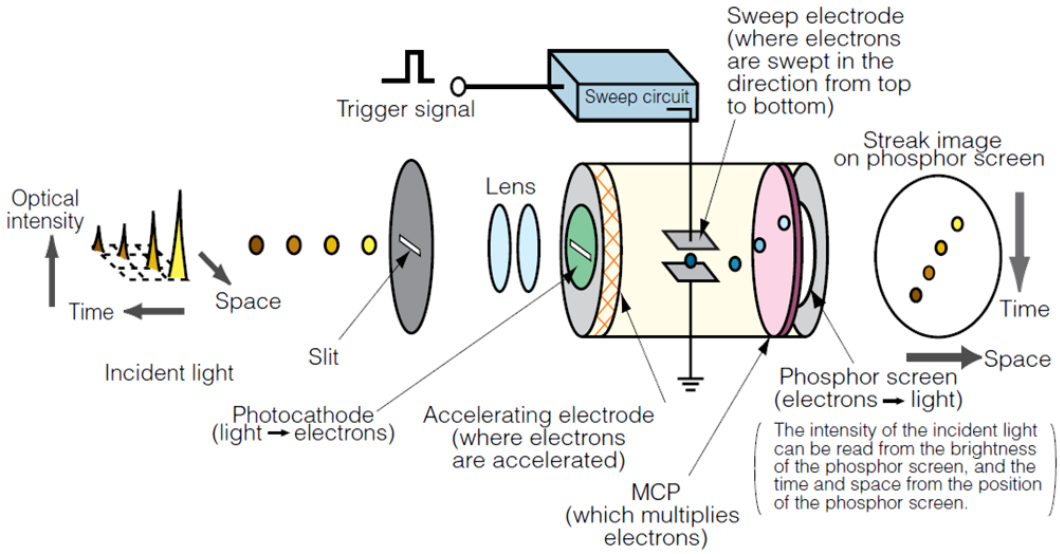

Figure 3-3 Operating principle of streak cameras [56].

3.5.2 C5680 Hamamatsu Streak Camera and Features of the Camera

In this research, we used a Hamamatsu C5680 streak camera, which can be used for many purposes by selecting an appropriate sweep unit and other function units. Adaptable sweep units for the camera are the single-sweep unit and the synchroscan sweep unit. In the single sweep mode, using the single-sweep unit, only one sweep is involved (single shot), and it is appropriate for single pulse measurements or pulses with a repetition rate of up to tens of kHz. The sweep range in this mode is from 60 ps to 10 ms.

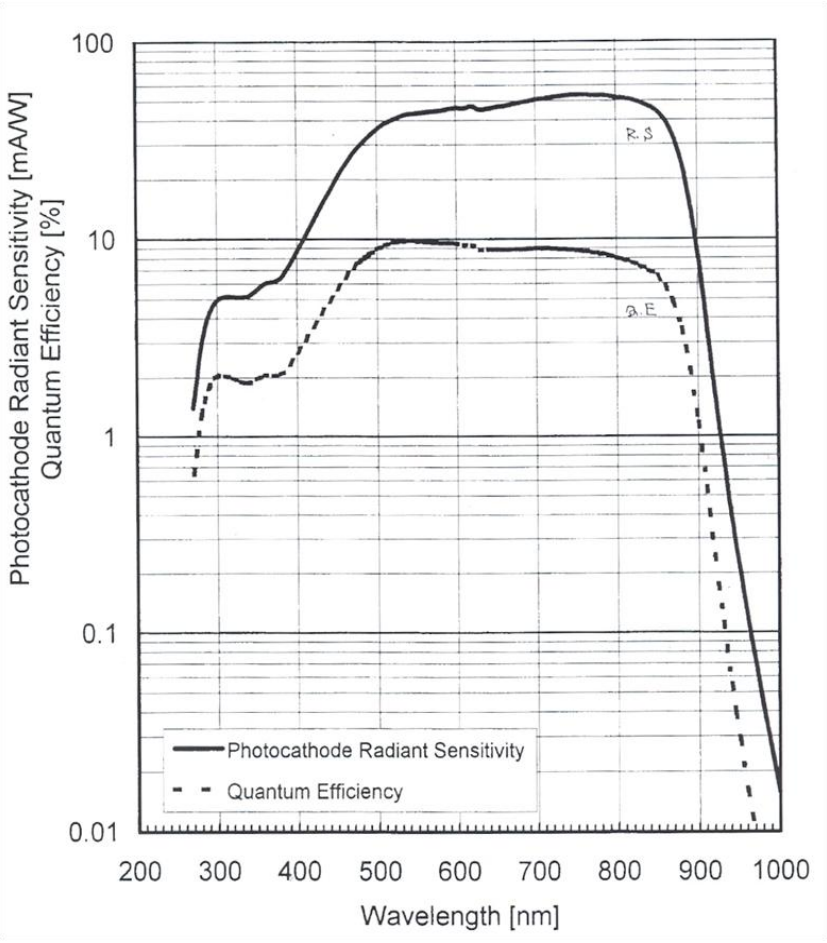

Figure 3-4 Photocathode radiant sensitivity of the C5680 streak camera for different wavelength [57, 58].

The synchroscan mode, using synchroscan sweep unit, is a high-speed repeated sweep. In this mode, the streak image can be integrated at a fixed position on the phosphor screen. Therefore, by using this unit, very faint optical events, even a few photons, can be

detected and measured. The repetition of the optical phenomenon is the same as the sweep frequency, which can be between 75 MHz to 165 MHz, based on the sweep model.

In this research, the streak camera was used to detect and measure the single photons produced form SHG at 400 nm wavelength. Figure 3-4 shows the radiant sensitivity graph of the photocathode of the C5680 streak camera at different wavelengths. At 400 nm wavelength, the streak camera is not in maximum sensitivity; however, it is still sensitive enough to detect the SH signal of our samples. To detect the SH signal, M5675 Hamamatsu synchroscan sweep unit was applied on the streak camera. The repetition rate of the unit was 90 MHz, which was matched with the repetition rate of Ti:Sapphire light source, and the sweep range was from 200 ps to 2 ns.

3.5.3 Principle of Photon Counting Integration

As we explained in prior subsections, photoelectrons which are given off from the photocathode of the streak tube are multiplied at the high integration rate by the MCP. The MCP is an electron multiplier which can multiply a single electron into as many as 1000. These photoelectrons are conducted to the phosphor screen. Each photoelectron is count as one intensity point on the phosphor screen, forming the streak image.

To separate the noise from streak image, a threshold value is applied. Therefore, only signals with intensity above the threshold value are detected and are integrated in the memory. This makes it possible achieve high separation between signal to noise. Figure 3-5(a) shows an example of setting a threshold value and separating the photoelectron image from background noise. Figure 3-5(b) shows a typical example of photon counting integration profile.

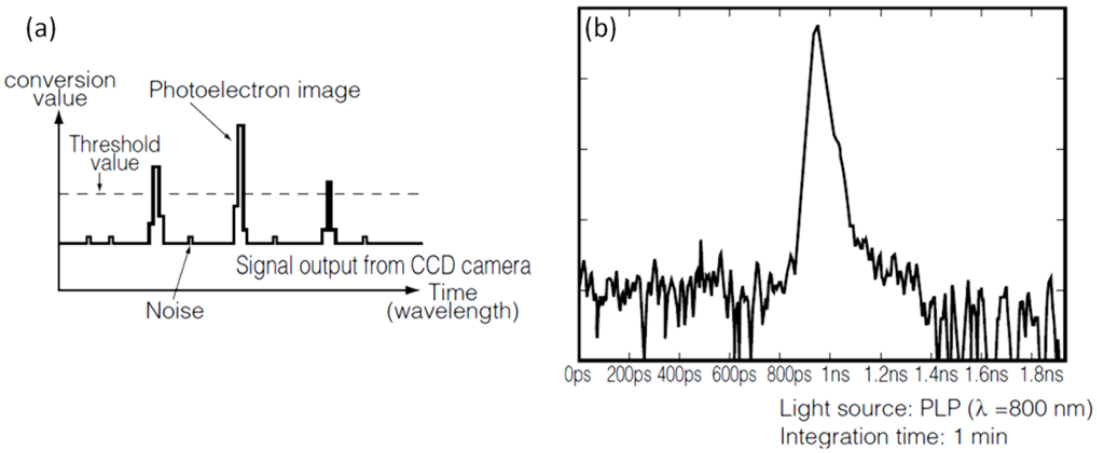

3-5 Example of setting a threshold value and separating signal from noise. (b) Typical example of photon counting profile [55].

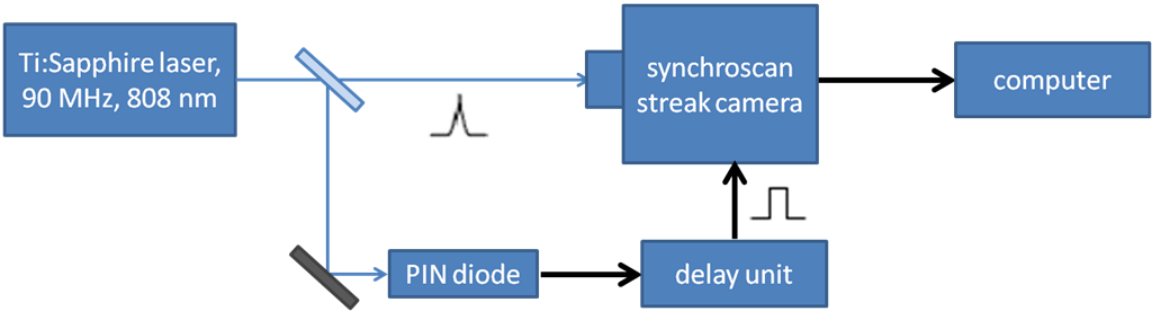

Figure 3-6 Setup configuration for photon counting measurement.

3.5.4 Photon Counting Measurement

Figure 3-6 shows the setup configuration of the photon counting measurement. Ti:Sapphire laser (90MHz repetition rate, maximum power at 808 nm) in mode-locked mode was used as excitation light source. To measure the incident light pulse in the streak camera, the sweeping time must be simultaneous with the input pulse after converting to photoelectrons. For this purpose, a small portion of laser light, between 3 mW to maximum 5 mW, is directed to a PIN photodiode (Hamamatsu C1808). The PIN photodiode converts the incident light pulse into the trigger signal for the synchroscan sweep unit. Figure 3-7 shows the output of the C1808 PIN photodiode on the oscilloscope in our setup. Also, to introduce and adjust the delay time in to the sweep unit, a delay unit can be used. This unit can adjust the delay time as small as 25 ps manually. In this research, we have used a Hamamatsu C1097 delay unit with time ranges

of 0.25 ns, 0.5 ns, 1 ns, 2 ns, 4 ns, 8 ns, and 16 ns. Figure 3-8 shows an image of our photon counting measurement setup with following components; (1) Ti:Sapphire laser. (2) Optical setup. (3) Input optics system of streak camera, including slit plate, focusing ring, lens. (4) Streak camera and synchroscan unit. (5) Delay unit. (6) Power supply unit. (7) Camera controller. (8) Computer.

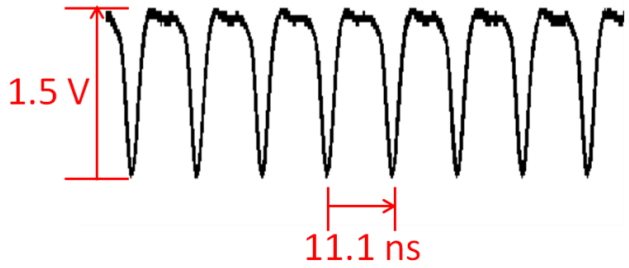

Figure 3-7 the output of the C1808 PIN photodiode on the oscilloscope in our photon counting setup.

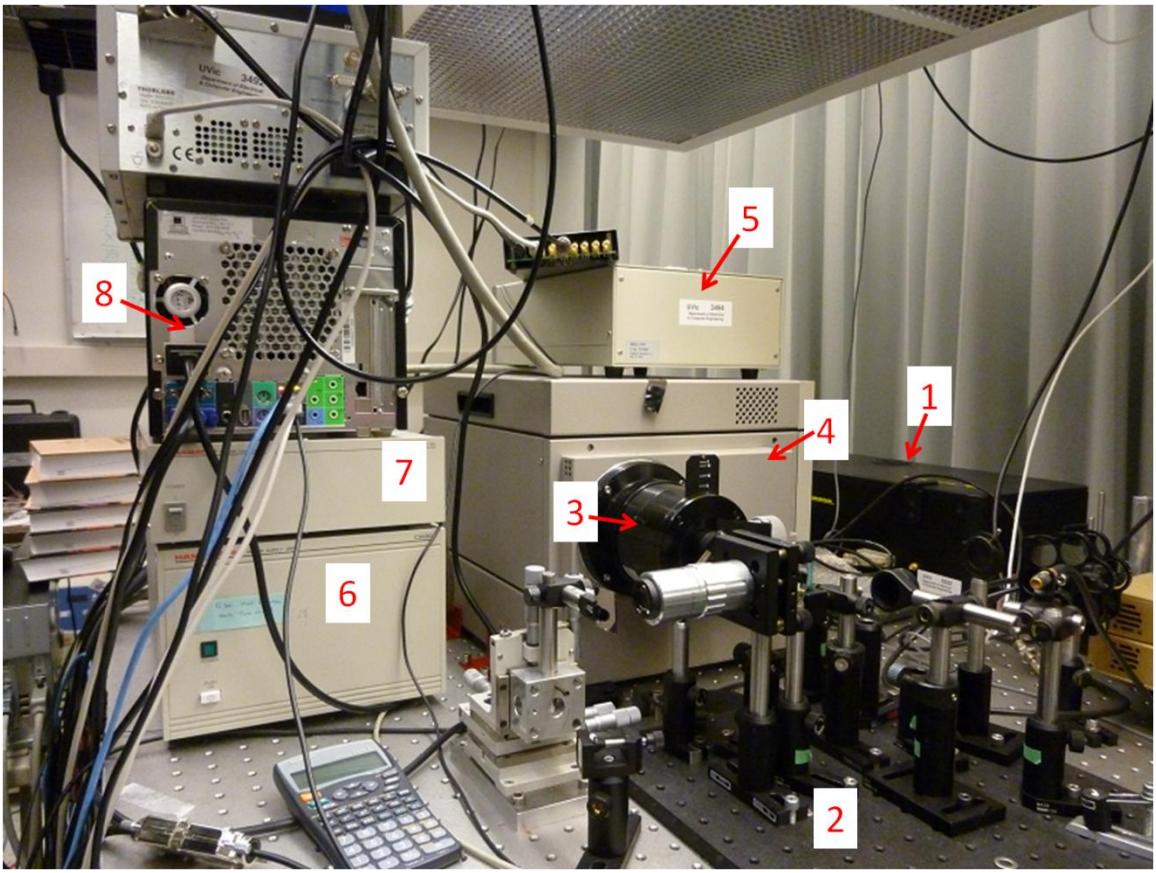

Figure 3-8 An image of photon counting measurement setup. (1) Ti:Sapphire laser. (2) Optical setup. (3) Input optics system of streak camera, including slit plate, focusing ring, lens. (4) Streak camera and synchroscan unit. (5) Delay unit. (6) Power supply unit. (7) Camera controller. (8) Computer.

Beside the manually adjustment of unit delay, all other adjustments are done via HPD-TA program. The HPD-TA program is a 32-bit software, supports the Hamamatsu streak cameras. The program can control the streak camera, acquisition, and displayed streak image. For example, opening and closing the shutter of the camera, selecting the operation mode of camera (for pre-adjustments and alignment of the incident light), setting the exposure interval and number of integrated exposures, MCP gain, triggering the internal delay (to set the image in the center of screen), and region of interest are controlled by the program.

For photon counting measurement, many adjustments must be done. Details of this process can be found in the HPD-TA user manual for streak camera [57, 58].

Figure 3-9 shows a typical screen layout of photon counting in our measurement.

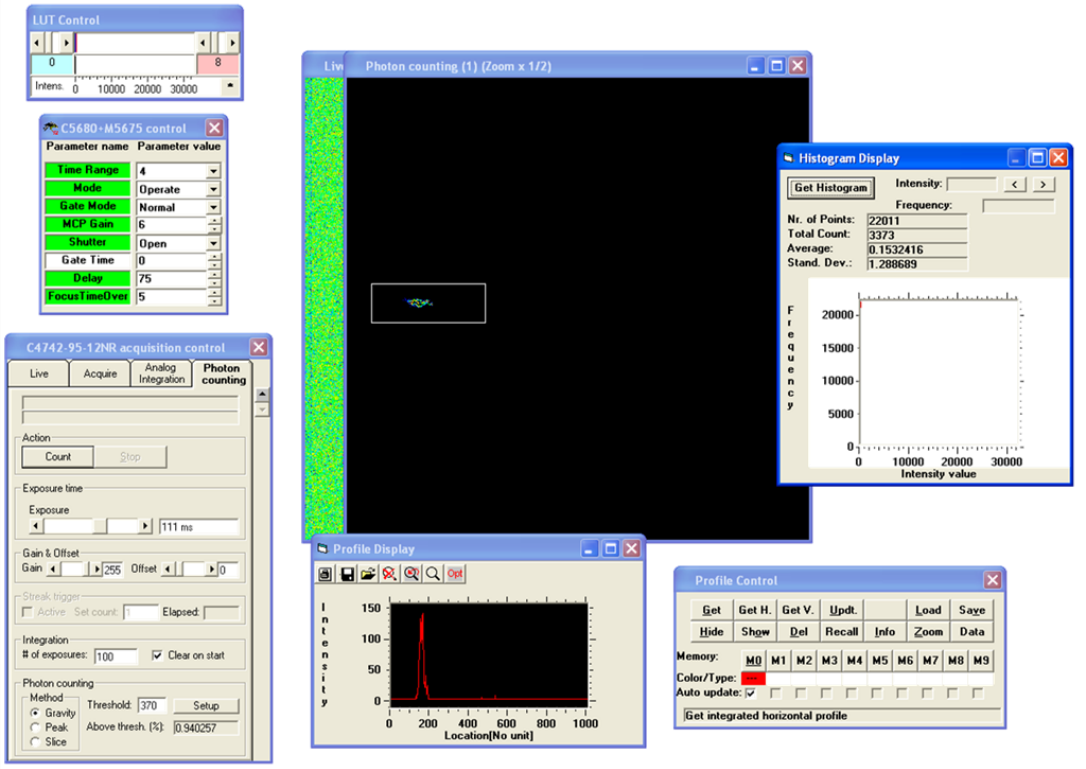

Figure 3-9 Screen layout of photon counting mode.

3.6 Summary

This Chapter provided an overview of the equipment used throughout my research. First, SEM as imaging instrument and UV-Vis spectrometry were briefly discussed. Next, working principles and features of Ti:Sapphire laser were explained. Last, a short description of streak camera in synchroscan mode was provided.

Chapter 4

4 Sample Preparation and Characterization

4.1 Introduction

This Chapter presents the fabrication methods and characterization details for both metal nanoparticles and hybrid systems.

4.2 Synthesis of Silver Nanoprisms

The silver nanoprism solution was prepared following the photoinduced conversion method of silver nanospheres to nanoprisms [47]. As a typical synthesis process, an aqueous solution of silver nitrate (0.1 mM, 100 ml), (204390, Aldrich Chemicals), and trisodium citrate (0.3 mM), (S2990, ACP Chemicals Inc.), was prepared in presence of air with a moderate stirring rate (~120 rpm). Next, sodium borohydride solution (50 mM, 100 ml), (7420-1, Caledon Laboratories Ltd.), was injected to the system. Following this, Bis (p-sulfonatophenyl) phenylphosphine dehydrate dipotassium salt (BSPP) (5 mM, 2 ml), (698539, Aldrich Chemicals), was dropped into the solution over 2 min. BSPP was used as a stabilizer agent. The system was irradiated with a 24 W halogen lamp (ser. 700, Sunnex Inc.) for 72 h. The reaction was terminated after 72 h irradiation. In dark-room, at room temperature condition, the final solution is stable for more than 6 months.

During the synthesis process, we observed changing in the solution's colour as Figure 4-1 shows. The clear initial solution of silver salt and citrate turned to yellow after the injection of the sodium borohydride which indicates the formation of silver nanospheres. During the irradiation process, the solution's colour turned to green and finally blue.

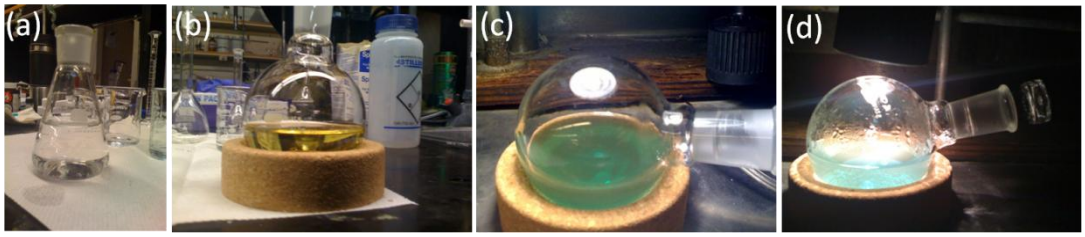

Figure 4-1 Colour of the solution was changed during the synthesis process. (a) and (b) Immediately after injecting sodium borohydride solution, clear colour of system turned to yellow which is characteristic of silver nanospheres. (c) and (d) During the irradiation process, yellow colour turned to green and finally blue.

4.2.1 Extinction Evaluation of Silver Nanoprisms in Aqueous Solution

To characterize nanoparticles during the reaction, the optical extinction of samples from the solution were monitored as a function of time with a Cary 5 UV-VIS-NIR spectrometer. Initial yellow solution shows a single SPR peak at 400 nm, as we expect for very small silver nanospheres. Figure 4-2 shows that after 17 h irradiation, these nanospheres were converted to nanoparticles with plasmon resonance at 330 nm (weak) and 600 nm (strong). Continuing irradiation for longer intervals, the long-wavelength extinction resonance was shifted to longer wavelength, while the reaction was terminated after 72 h irradiation with final nanoprisms with a 87±13 nm edge length (uncertainty is standard deviation σ), a 6 nm radius of curvature at the edges, and 12 nm thickness, and the plasmon resonance at 330 nm (weak), 500 nm (medium), and 680 nm (strong) (see Figure 4-4(c)). Equation (4.1) and the SEM image (Figure 4-3(d)) were used to obtain the edge length and standard deviation σ of the nanoprisms.

$$\sigma = \sqrt{\frac{1}{N}\sum_{N}^{i}(x_i - \mu)^2} \tag{4.1}$$

where μ is:

$$\mu = \frac{1}{N}\sum_{N}^{i} x_i \tag{4.2}$$

According to the literatures [47], the 680 nm peak is corresponded to the in-plane dipole plasmon resonance, the 500 nm peak is in-plane quadrupole resonance, and 330 nm peak is out-of-plane dipole resonance. The reminder of this work, including SEM samples, atomic force microscopy (AFM) samples, and hybrid systems, is based on final silver nanoprisms with resonance at 680 nm.

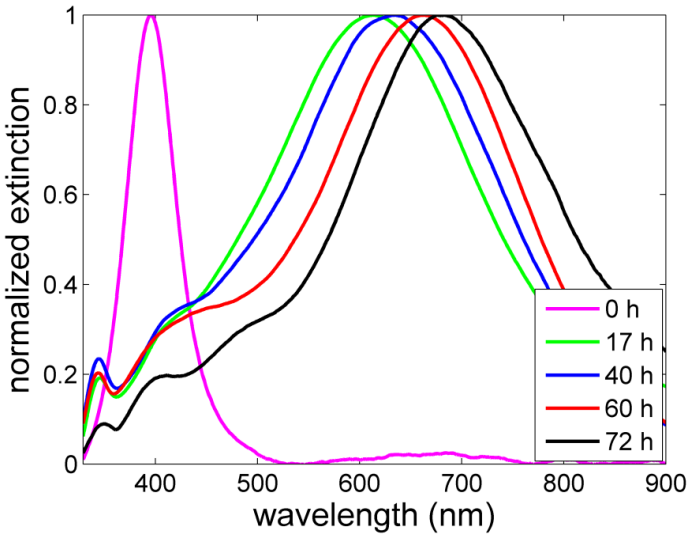

Figure 4-2 Evaluation extinction of silver nanoparticles in aqueous solution as a function of irradiation time.

4.2.2 SEM Characterization

Figure 4-3 shows a SEM images of typical silver nanoprisms after 72 h irradiation on gold substrate (Figures 4-3(a), 4-3(b), and 4-3(c)) and on silicon wafer (Figure 4-3(d)). To prepare substrates for SEM and AFM imaging, the silver nanoprisms were spin-coated onto the (1 cm **x** 1 cm) substrate at 700 rpm for 90 sec (1 drop of the undiluted solution).

4.2.1 AFM Characterization

Figures 4-4(a) and 4-4(b) shows an AFM scan (Agilent 5500) in AC mode of the silver nanoprisms dispersed onto a silicon substrate with different zooms. The height was measured to be 12 nm (Figure 4-4(c)).

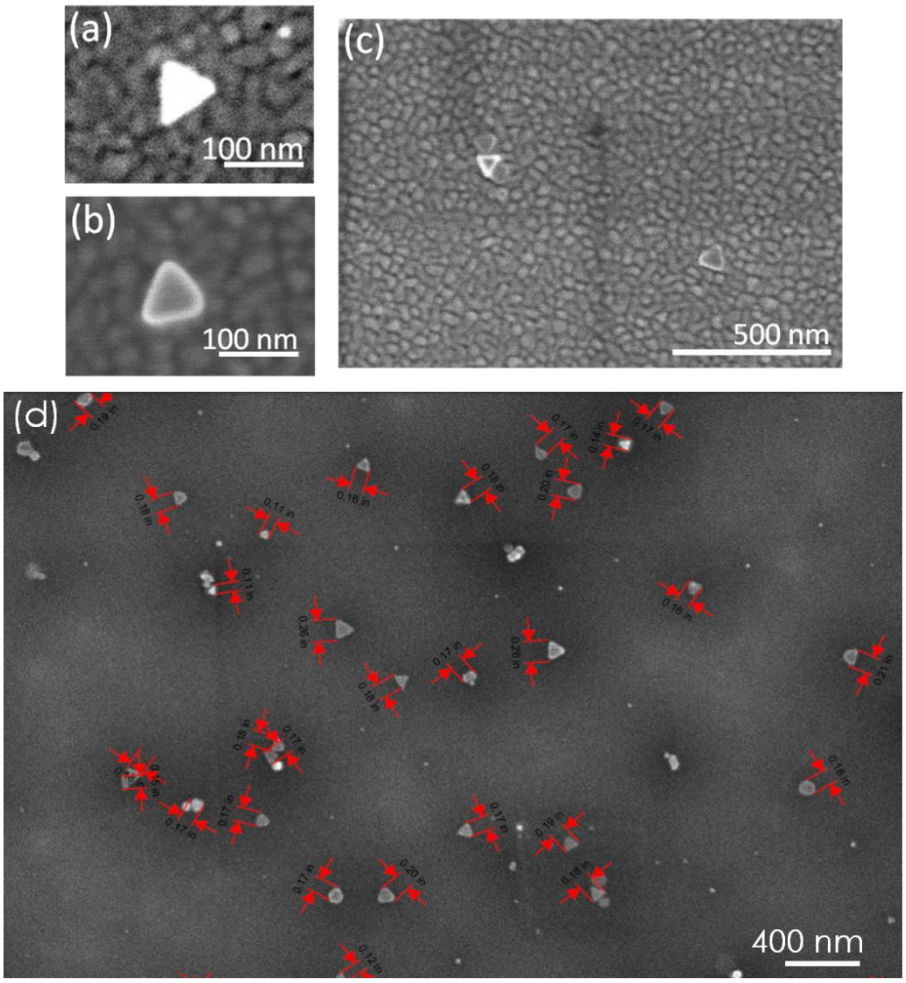

Figure 4-3 Scanning electron microscopy of silver nanoprisms with plasmon resonance at 680 nm spin-coated onto, (a), (b), and (c) the gold substrate, (d) the silicon wafer substrate. The edge length and the standard deviation was calculated 87±13 nm. [The SEM image in silicon is provided by J. Massey-Allard of UBC].

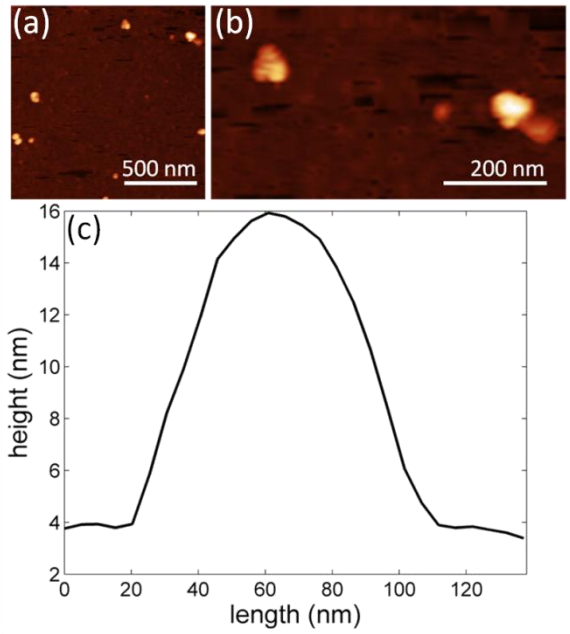

Figure 4-4 (a) and (b) AFM characterization of silver nanoprisms spin-coated on a silicon substrate. (c) The height of a typical silver nanoprism was measured to be 12 nm with AFM in AC mode.

4.3 Hybrid Systems

4.3.1 Fabrication of Hybrid Systems

We fabricated hybrid plasmonic systems by coupling silver nanoprisms with a thin gold film. Varying thicknesses of poly methyl methacrylate (950 PMMA A2, MicroChem) were used as dielectric spacer between nanoprisms and thin gold film. Figure 4-5 shows an illustration of the silver nanoprisms, spacer layer, thin gold film and glass substrate.

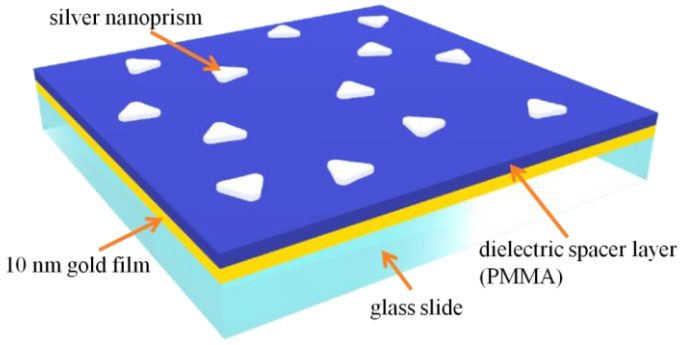

Figure 4-5 An illustration of silver nanoprisms with PMMA spacer layer over a 10 nm thick gold film adhered to a glass substrate with a 2 nm titanium layer (is not shown in the Figure 4-5).

Commercial substrates were used consisting of a 10 nm thick gold film with a 2 nm titanium adhesion layer on glass (AU.0100.CSS, Platypus Technologies). The commercial substrate had a flat and continuous film, even for 10 nm thickness, and we could achieve similar quality only by evaporating gold films with the substrate temperature elevated to 200˚C or more; however, the remainder of this work is based entirely on samples prepared with the commercial substrates. The spacer layer was created by spin-coating PMMA at 3500 rpm for 90 sec with varying anisole (296295, Sigma-Aldrich) solvent concentration to achieve varying post-baking thicknesses between 5 nm and 20 nm [59]. The PMMA on substrate was baked for 5 min at 180˚C. Following this, the silver nanoprisms were spin-coated onto the substrate at 700 rpm for 90 sec (1 drop of the undiluted solution). The surface coverage density was 120 nanoprisms per 60 μm^2, assuring a good statistical average in the SHG measurements in Chapter 6.

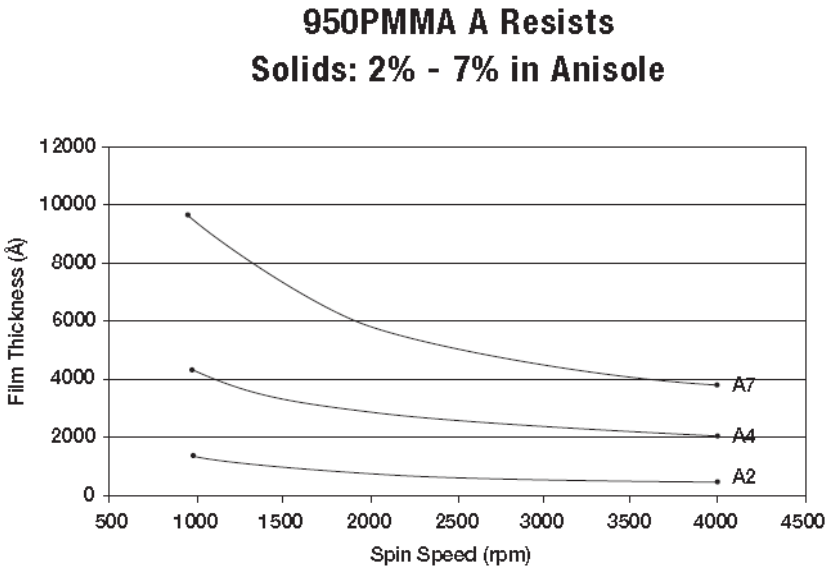

Figure 4-6 PMMA film thickness (Å) as a function of spin speed (rpm) [59].

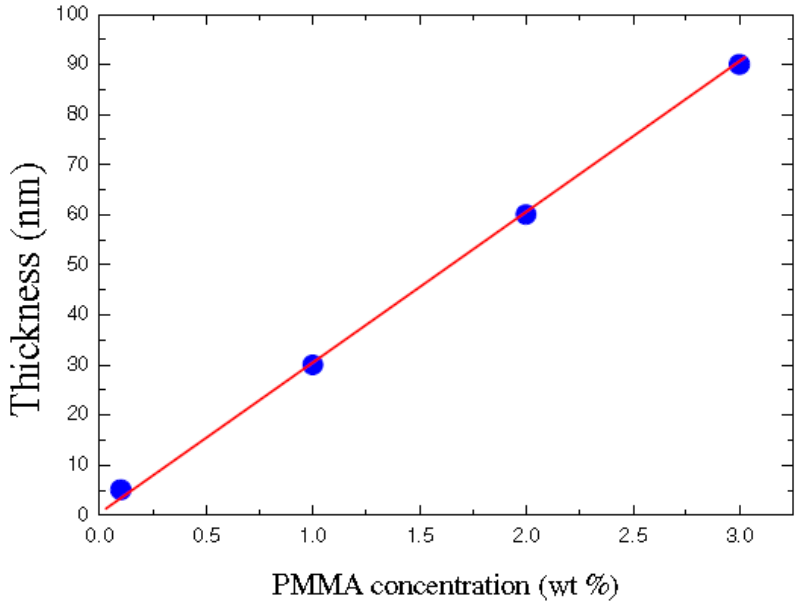

Figure 4-7 PMMA thickness (nm) as a function of PMMA concentration (wt%) specifically at 3500 rpm for 90 sec. Reprinted with permission from [60]. Copyright © 2009 American Chemical Society.

4.3.2 Spin-Coating PMMA Thin Film with Various Thicknesses

Figure 4-6 shows PMMA film thickness (Å) as a function of spin speed (rpm). Figure 4-7 shows PMMA thickness (nm) as a function of PMMA concentration (wt%), specifically at 3500 rpm for 90 sec [60]. I used these data to get an accurate relation between different concentrations of PMMA and thicknesses of PMMA film. All hybrid systems were prepared using 950 PMMA 2% solution. To dilute 100 µl of the original PMMA solution, necessary volume of anisole was calculated applying this equation:

$$M_i V_i = M_f V_f \tag{4.3}$$

where M is the concentration of PMMA, and V is volume of solution, including PMMA and anisole, and the subscripts i and f refer to initial and final values, respectively. Table 1. lists the anisole volumes, final PMMA concentration and final thickness of PMMA baked layer. The dilution process was done by using 10 – 0.5 µl and 1000 – 100 µl micropipettes (Eppendrof Reference). For spin-coating process, a Laurell Technologies WS-650SZ-6NPP / A1 / AR1 Spin-Coat System was used.

Table 1. Spin-coating PMMA thin layer with different thicknesses. Volume of added anisole to 100 µl PMMA 2%, concentration of final PMMA, and final thickness of PMMA film after baking for 3500 rpm, 90 sec spin-coating condition.

Anisole volume (µl)	**PMMA concentration (wt %)**	**Final thickness of PMMA film (nm)**
912	0.198	5
495	0.336	8.5
406	0.395	10
340	0.454	11.5
237	0.593	15
153	0.790	20

4.4 Summary

This Chapter provided the fabrication methods and characterization details for both metal nanoparticles and hybrid systems used in my research. Synthesis and characterization methods of silver nanoprisms were explained. Also, the fabrication process of the hybrid plasmonic system has been detailed.

Chapter 5

5 Scattering of hybrid system

5.1 Introduction

This Chapter describes the linear optical response of hybrid plasmonic systems. The experimental setup and measurements, as well as the simulation details, are provided.

5.2 Scattering Measurement

5.2.1 Experimental Setup

Figure 5-1 shows an illustration of the scattering measurement setup. A halogen WLS (LS-1-LL, Ocean Optics Inc.) was focused into the side of the sample by a 20× microscope objective (Mitutoyo Plan Apo, Edmund Optics Inc.), allowing for waveguiding in the sample. The scattered light at the surface of the sample (where the nanoprisms and metal film were located) was collected normal to the surface by an optical fiber (0.22 NA) and the spectrum was recorded using a spectrometer (QE65000, Ocean Optics Inc.).

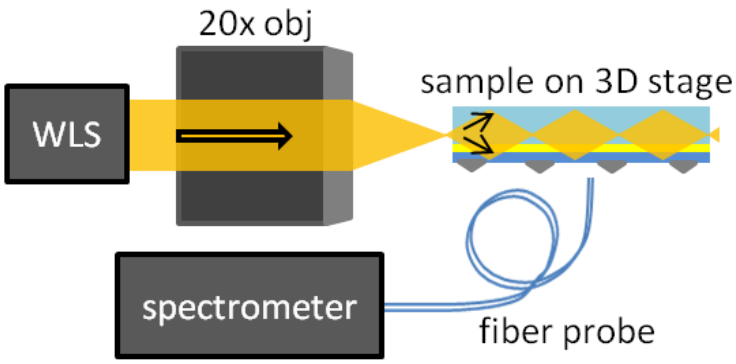

Figure 5-1 An illustration of scattering measurement setup. WLS= white light source, obj= microscope objective lens.

5.2.2 Scattering FDTD Simulation

The proposed structure was simulated using a commercial finite-difference time-domain simulation package (FDTD ver. 7.5.7, Lumerical Solutions Inc.) to estimate the scattered power and local field enhancement (Figure 5-2). For accurate modeling of the structure, a mesh size of 1.5 nm was used. The simulation domain was terminated with a perfectly matched layer for minimal reflection. The complex permittivities of gold and

silver were modeled using the experimental data of Johnson and Christy [61] and Palik [62], respectively. For the PMMA spacer layer, a refractive index of 1.5 was used. The silver nanoprisms were modeled with a rounded edge radius of 6 nm. The source was polarized along the axis of symmetry of the silver nanoprism in the *x* direction (see Figures 6-5(a) and 6-5(c)). To calculate the scattered power, we employed the formalism of total field scattered field. A set of two-dimensional power monitors was used, enclosing the nanoprism. The total power exiting this closed surface represents the scattered power. Also, we used a two-dimensional frequency domain field profile monitor to determine the near-field intensity distribution.

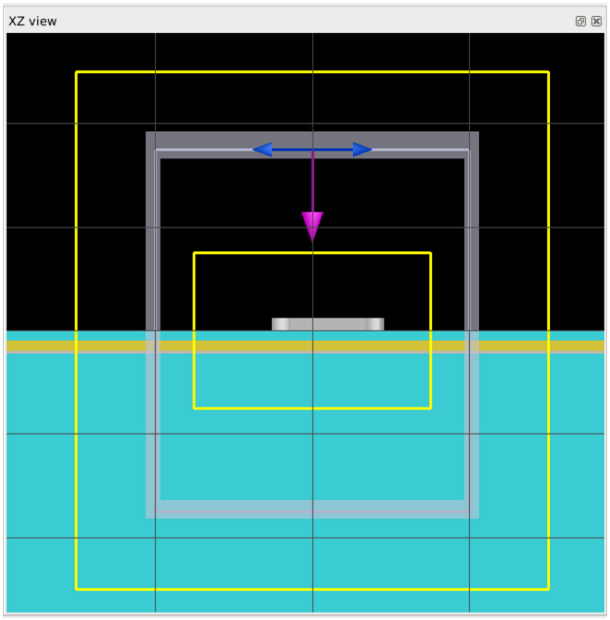

Figure 5-2 FDTD simulation to estimate the scattered power and local field enhancement of the proposed hybrid system (silver nanoprism-PMMA spacer layer-10 nm gold film-2 nm titanium adhesion layer-glass micro slide). The gray box: source, total field scattered field (TFSF). Pink arrow: propagation direction. Blue arrows: Polarization direction, along the symmetric axis of silver prism. Yellow boxes: monitors.

5.2.3 Scattering Measurements

Figure 5-3 shows scattering measurements for three different spacer layer thicknesses. Figure 5-3(a) shows the experimental results, as well as the Ti:Sapphire laser spectrum (dashed-dot green line), to compare the peak position of light source and the hybridized

resonances. Figure 5-3(b) shows the FDTD simulation results for silver nanoprisms for the corresponding spacer thicknesses.

Figures 5-4 shows the experimental and simulation scattering peak wavelength for the hybrid plasmonic system (Ag-PMMA-Au-Ti-glass) as a function of PMMA thickness for additional thicknesses. Good agreement is seen between the measured scattering peak, and the one obtained by FDTD calculations. It is clear from Figures 5-3 and 5-4 that we can tune the plasmonic resonance through the peak wavelength of the Ti:Sapphire laser (808 nm) by plasmon hybridization. Since the linear response gives the largest scattering at the peak wavelength of the Ti:Sapphire laser for a PMMA thickness of 10 nm, we expect that the local field enhancement, and hence SHG, will be greatest for that thickness too.

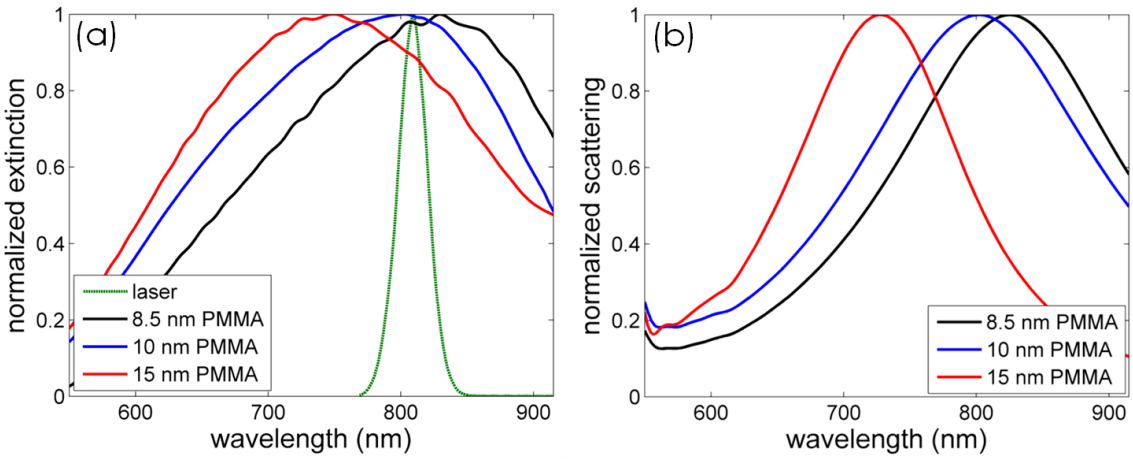

Figure 5-3 Normalized scattering measurements and simulations. (a) Scattering measurement for three hybrid structures with different PMMA spacer layer thicknesses (shown in legend). Green dashed line: Ti:Sapphire spectrum. (b) Scattering simulation results for silver nanoprisms for the corresponding spacer thicknesses.

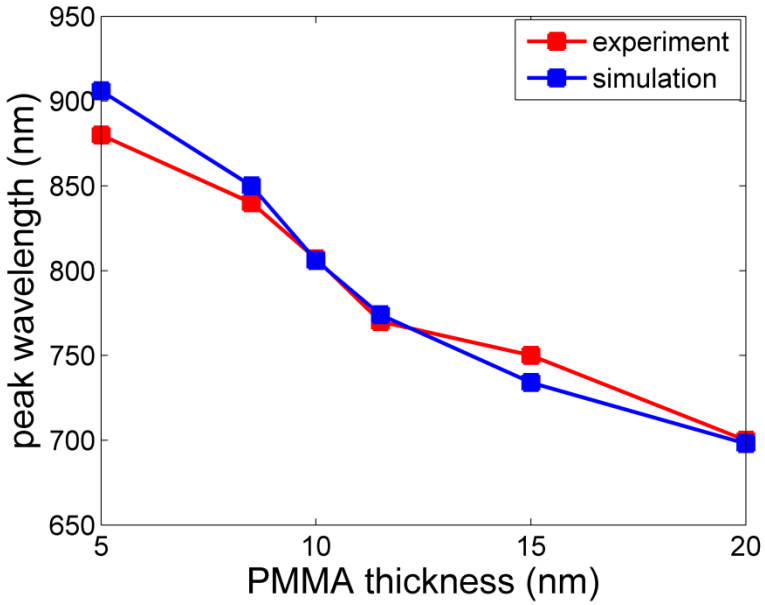

Figure 5-4 Peak scattering wavelength as a function of PMMA spacer layer thickness from experiment and FDTD simulations.

5.3 Summary

This Chapter discussed the linear optical response of plasmonic hybrid systems. The plasmonic resonances in the silver prisms with the gold film allows for spectral tuning of the hybrid mode. The resonance frequency of the excited mode can be finely adjusted via the spacer layer thickness.

Chapter 6

6 SHG Measurements

6.1 Introduction

This Chapter describes the experiments carries out for the nonlinear optical response of the hybrid systems. Also, near-field simulation details are provided for comparison.

6.2 SHG Experimental Setup

Figure 6-1 shows an illustration of the SHG detection setup. A Ti:sapphire laser with was used to produce ~25 fs pulses with center wavelength of 808 nm and a repetition rate of 90 MHz. The applied average power was tuned via neutral density (ND) filters, while the maximum average power was limited to 30 mW. The laser light was focused onto the sample with off-axis illumination using a 20× long working distance microscope objective (Mitutoyo Plan Apo, Edmund Optics Inc.) to produce a 60 μm^2 spot area. The spot area was measured using a CMOS camera (DCC1645C, Thorlabs Inc.) (Figure 6-2(a)). The average power was measured at the same location as the sample. The reflected laser light was blocked with an off-axis metal stop, and the normal emission beam, containing the SHG and scattered fundamental beam, was guided to a streak camera (C5680, Hamamatsu) with a 45° cold mirror (FM04, Thorlabs Inc.), passing through a bandpass BG40 filter to remove the fundamental beam with the expense of 30% of second harmonic signal. The streak camera was operated in synchroscan (M5675, Hamamatsu) photon-counting mode with microchannel plate gain of 6, in a manner similar to our previous work, as described in Chapter 4 [63-65].

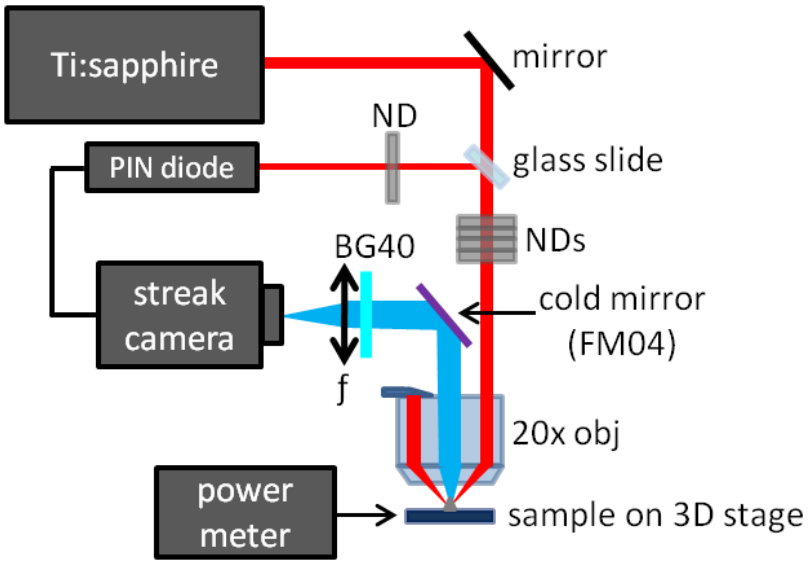

Figure 6-1 An illustration of SHG measurement setup. ND = neutral density filter, obj = microscope objective lens, BG40 = blue-green band pass filter.

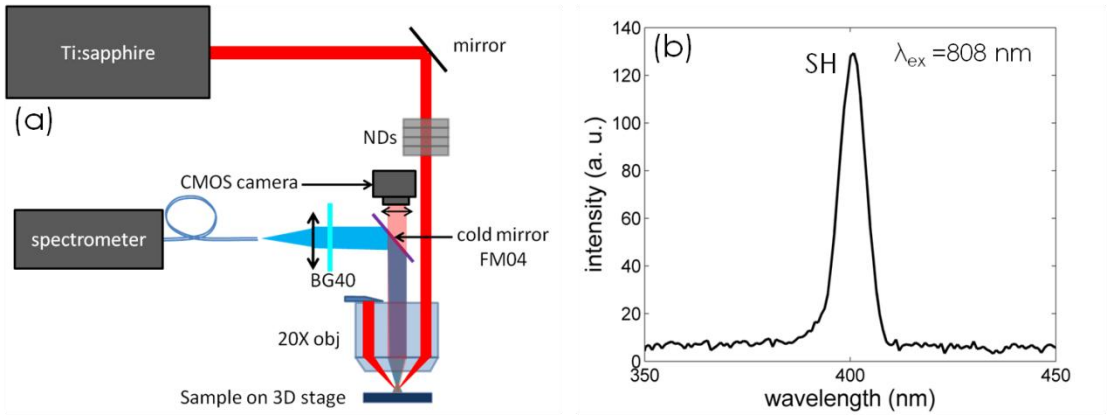

Figure 6-2(a) Schematic of second harmonic spectrum measurement setup. The SHG spectrum was taken from in front of the streak camera using the fiber-probe spectrometer. (b) The measured SH spectrum.

6.2.1 SHG Measurement

Figure 6-2(a) shows the measured second harmonic spectrum, taken from in front of the streak camera using the fiber-probe spectrometer (Figure 6-2(b)). Figure 6-3 shows the SHG counts as a function of PMMA thickness for 30 mW incident power. The maximum value obtained was 9000±240 (error from standard deviations over 10 runs at different locations on the sample) for 10 nm thickness. By comparison, for a sample of silver nanoprisms on a glass microslide alone, the SHG was 14±4. This shows that the enhancement factor of the SHG was approximately three orders of magnitude. Figure 6-4

shows a log-log plot of the SHG versus incident laser power for the 10 nm thickness sample for four different incident powers. The experimental measured data were fitted to a straight line with polynomial cure fitting function. The slope S of the fitting line was calculated as below:

$$S = \sqrt{\frac{\sum(y_i - ax_i - b)^2}{n-2}} \quad (i = 1, 2, 3, 4) \tag{6.1}$$

$$y = ax + b \tag{6.2}$$

where n is the number of experimental data points, x is independent variable (here, $\log_{10}$ of the incident power for each experimental data point), y is dependent variable (here, $\log_{10}$ of the SHG count for each experimental data point), and the subscript i refers to x and y values for each experimental point, and a and b give relation between x and y. For polynomial carve fitting $a = 2.1665$ and $b = 0.7704$. The slope of fitting line is obtained 2.17. The uncertainty, Error, was calculated ±0.20 using the following equation:

$$Error = S \times \sqrt{\frac{n}{(n\sum x_i^2) - (\sum x_i)^2}} \tag{6.3}$$

Therefore, the slope of fitting line was obtained 2.17±0.20. Considering the SHG process a slope of 2 is expected, which is in reasonable agreement with the data.

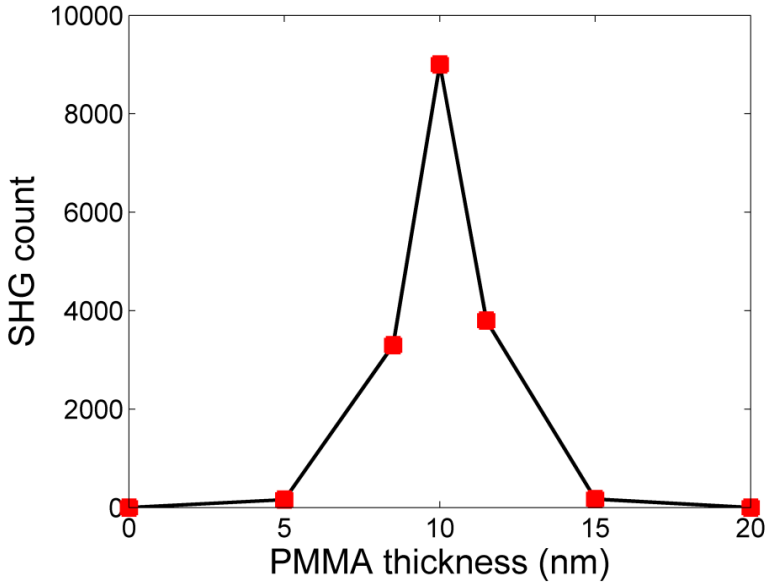

Figure 6-3 SHG count dependence on PMMA spacer layer thicknesses for 30 mW average incident power at sample spot.

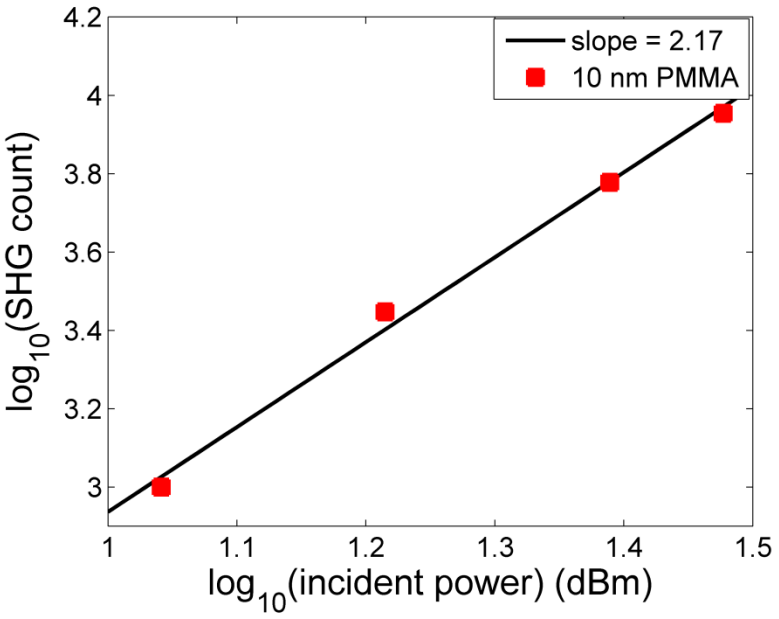

Figure 6-4 Log-log plot of SHG count vs. incident laser power with polynomial carve-fit slope of 2.17±0.2. For SHG, a slope of 2 is expected.

6.2.2 Near-Field Enhancement Simulation

To see if the experimentally observed 3-order of magnitude enhancement is reasonable from a theoretical point of view, we considered FDTD calculations. Figure 6-5 shows FDTD calculations of the near-field intensity (wavelength of 808 nm) for a silver nanoprism hybridized with a 10 nm gold film, with 10 nm PMMA spacer layer. This calculation gives a maximum enhancement of 1420× the incident intensity. By comparison, we have made a similar calculation for a silver nanoprism on glass and found that the maximum enhancement is 82× the incident intensity. Therefore, the hybridization process has a net enhancement of 17.3× in the field intensity, and since the SHG scales as the square, this corresponds to 300× in the SHG generation, which is half what was seen in the experiments. While this is reasonable agreement considering the accuracy of numerical calculations, we note that the thin metal film may actually direct the SHG light into the detector, and thereby boost the signal in the experiments [66-68]. We have not accounted for this effect in the calculations. While there is some enhancement from gap plasmons in our structure [69-71], these are not dominant, as can be seen from the field distribution in the calculations (Figure 6-5(b)).

We also performed calculations for 680 nm wavelength and found an even greater near-field enhancement for the silver nanoprism on glass (i.e. without hybridization); therefore, the hybridization does not improve the near-field enhancement on resonance. In other words, if a source is available at 680 nm, it would be better to use that source with a non-hybridized system. The main function of the hybridization then was to tune the resonance to the wavelength of the common Ti:Sapphire source.

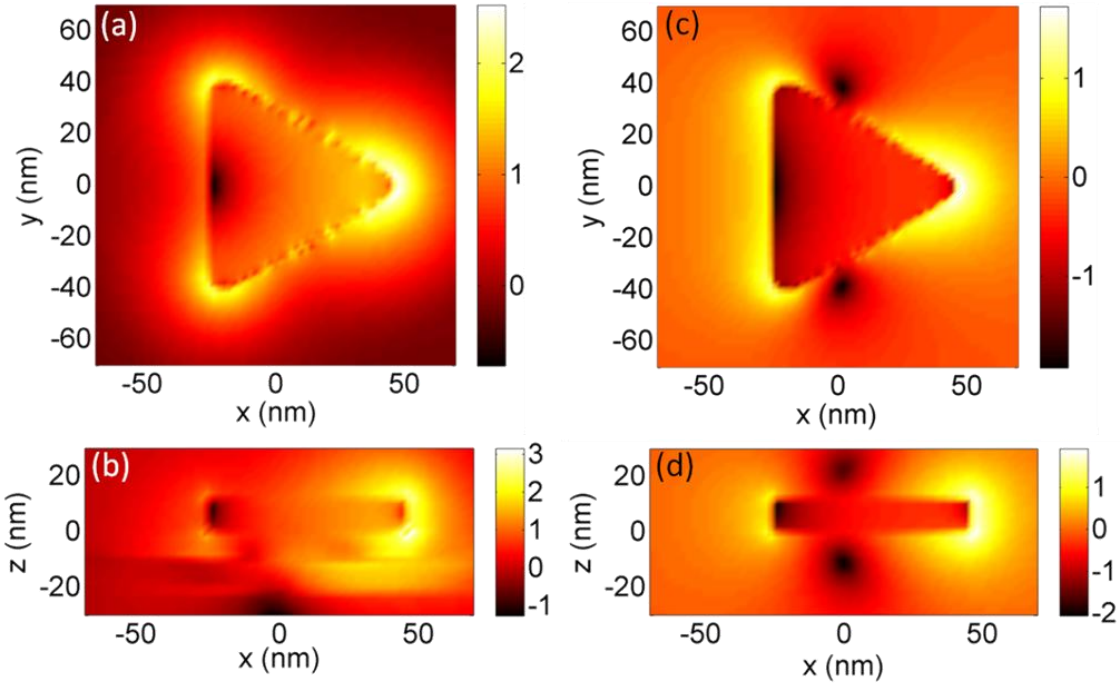

Figure 6-5 Near field map of the electric field intensity, (a) and (b) for a silver nanoprism on 10 nm PMMA, 10 nm gold, 2 nm Ti, glass substrate, at the source wavelength of 808 nm in (a) *xy* and (b) *xz* planes. (c) and (d) Show the same distribution for a silver nanoprism on glass substrate, at the source wavelength of 808 nm in (c) *xz* and (d) *xz* planes. The scale bar is logarithmic (base 10).

6.3 Summary

This Chapter described the experiments carried out for the nonlinear optical response of the hybrid plasmonic systems. The SHG was maximum for the hybrid system with the best overlap of the driving laser source and the plasmon resonance. Also, near-field simulation details were provided for comparison.

Chapter 7

7 Summary and Future Work

7.1 Summary of Results

In conclusion, we have demonstrated that plasmon hybridization of metal nanoprisms to a thin metal film is an effective method for SHG enhancement of close to three orders of magnitude. The enhancement comes from fine tuning of the hybrid resonance to coincide with the excitation source.

7.2 Future Work

In the future, it would be interesting to apply these findings to enhanced multi-photon lithography [1], quantum dots coupling [60], high-harmonic generation [72], and nonlinear sensing [73].

7.2.1 Quantum dot Coupling and Two-photon Lithography

For the next step of the project, coupling a semiconductor single quantum dot (QD) to a silver nanoprism on the hybrid structure is required. The coupling of a semiconductor QD to plasmon particle can lead to emission of the QD as a single-photon emitter [60].

In general, there are two main issues with coupling a single QD to a metal nanoparticle; first, allocating only a single QD to a prism; second, tuning the plasmon resonance of the prism with emission wavelength of the QD.

To allocate a single QD to one silver prism, the SHG from the plasmonic hybrid system is used for two-photon lithography [1]. Moreover, in the hybrid structure precise tuning of the plasmon resonance of silver nanoparticle to the emission wavelength of QD is possible.

Chapter 8

8 Appendix

8.1 Moving Silver Nanoprisms on a Substrate

In a parallel project, the prepared silver nanoprisms were used to couple with a photonic crystal by J. Massey-Allard of UBC. This required moving the silver prisms and placing them onto the center of the photonic crystal. AFM has been used to move a prism. However, the stabilizer agent of the silver nanoprisms, BSPP, makes problem in moving process. BSPP is an organic, captivating the prisms (Figure 8-1). In case that silver nanoprisms are in a solution, centrifuging of the solution can help to remove the exceeding BSPP from it. In the case that silver nanoprisms are coated onto a substrate, washing the substrate with DI water can remove the BSPP from the substrate.

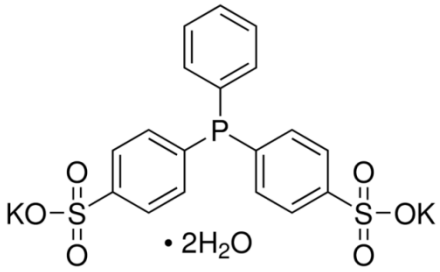

Figure 8-1 Molecular formula of BSPP [74].

Bibliography

[1] G. Volpe, et al., "Near-field mapping of plasmonic antennas by multiphoton absorption in poly(methyl methacrylate)," *Nano Letters,* vol. 12, pp. 4864-4868, 2012.

[2] A. K. Singh, et al., "Nonlinear optical properties of triangular silver nanomaterials," *Chemical Physics Letters,* vol. 481, pp. 94-98, 2009.

[3] J. Butet, et al., "Optical second harmonic generation of single metallic nanoparticles embedded in a homogeneous medium," *Nano Letters,* vol. 10, pp. 1717-1721, 2010.

[4] T. Xu, et al., "Second-harmonic emission from sub-wavelength apertures: Effects of aperture symmetry and lattice arrangement," *Optics Express,* vol. 15, pp. 13894-13906, 2007.

[5] K. Thyagarajan, et al., "Enhanced second-harmonic generation from double resonant plasmonic antennae," *Optics Express,* vol. 20, pp. 12860-12865, 2012.

[6] B. K. Canfield, et al., "Local field asymmetry drives second-harmonic generation in non-centrosymmetric nanodimers," *Nano Letters,* Vol. 7, pp. 1251-1255, 2007.

[7] Y. Zhang, et al., "Three-dimensional nanostructures as highly efficient generators of second harmonic light," *Nano Letters,* Vol. 11, pp. 5519-5523, 2011.

[8] R. Jin, et al., "Correlating second harmonic optical responses of single Ag nanoparticles with morphology," *Journal of the American Chemical Society,* vol. 127, pp. 12482-12483, 2005.

[9] P. Mühlschlegel, et al., "Resonant optical antennas," *Science,* vol. 10, pp. 1607-1609, 2005.

[10] P. J. Schuck, et al., "Improving the mismatch between light and nanoscale objects with gold bowtie nanoantennas," *Physical Review Letters,* vol. 94, pp. 017402-017405, 2005.

[11] H. Aouani, at al., "Multiresonant broadband optical antennas as efficient tunable nanosources of second harmonic light," *Nano Letters,* vol. 12, pp. 4997–5002, 2012.

[12] S. Linden, et al., "Collective effects in second-harmonic generation from split-ring-resonator arrays," *Physical Review Letters,* vol. 109, pp. 015502-015506, 2012.

[13] M. Hentschel, et al., "Quantitative modeling of the third harmonic emission spectrum of plasmonic nanoantennas," *Nano Letters,* vol. 12, pp. 3778-3782, 2012.

[14] T. Hanke, et al., "Tailoring spatiotemporal light confinement in single plasmonic nanoantennas," *Nano Letters,* vol. 12, pp. 992-996, 2012.

[15] K.-H. Su, et al., "Interparticle coupling effects on plasmon resonances of nanogold particles," *Nano Letters,* vol. 3, pp. 1087-1090, 2003.

[16] P. Nordlander, et al., "Plasmon hybridization in nanoparticle dimers," *Nano Letters,* vol. 4, pp. 899-903, 2004.

[17] A. M. Funston, et al., "Plasmon coupling of gold nanorods at short distances and in different geometries," *Nano Letters,* vol. 9, pp. 1651-1658, 2009.

[18] P. Nordlander and E. Prodan, "Plasmon hybridization in nanoparticles near metallic surfaces," *Nano Letters,* vol. 4, pp. 2209-2213, 2004.

[19] E. Prodan, et al., "A hybridization model for the plasmon response of complex nanostructures," *Science*, vol. 302, pp. 419-422, 2003.
[20] W. L. Barnes, et al., "Surface plasmon subwavelength optics," *Nature*, vol. 424, pp. 824-830, 2003.
[21] D. Y. Lei, et al., "Revealing plasmonic gap modes in particle-on-film systems using dark-field spectroscopy," *ACS Nano*, vol. 6, pp. 1380-1386, 2012.
[22] J. J. Mock, et al., "Probing dynamically tunable localized surface plasmon resonances of film-coupled nanoparticles by evanescent wave excitation," *Nano Letters*, vol. 12, pp. 1757-1764, 2012.
[23] M. Hu, et al., "Single particles spectroscopy study of metal-film-induced tuning of silver nanoparticle plasmon resonances," *Journal of Physical Chemistry C*, vol. 114, pp. 7509-7514, 2011.
[24] C. Lumdee, et al., "Post-fabrication voltage controlled resonance tuning of nanoscale plasmonic antennas," *ACS Nano*, vol. 6, pp. 6301-6307, 2012.
[25] F. Le, et al., "Plasmonic interactions between a metallic nanoshell and a thin metallic film," *Physical Review B*, vol. 76, pp. 165410-165422, 2007.
[26] O. Benson, "Assembly of hybrid photonic architectures from nanophotonic constituents," *Nature*, vol. 480, pp. 193-199, 2012.
[27] S. Hayashi and T. Okamota, "Plasmonics; visit the past to know the future," *Journal of Physics D: Applied Physics*, vol. 45, pp. 433001-43025, 2012.
[28] K. A. Willets and R. P. Van Duyen, "Localized surface plasmon resonance spectroscopy and sensing," *Annual Review of Physical Chemistry*, vol. 58, pp. 267-297, 2007.
[29] R. H. Ritchie, "Plasma losses by fast Electrons in thin films," *Physical Review*, vol. 106, pp. 874-881, 1957.
[30] C. J. Powell and J. B. Swan, "Origin of the characteristic electron energy losses in aluminum," *Physical Review*, vol. 115, pp. 869-875, 1959.
[31] L. Novotny and B. Hecht, *Principles of the nano-optics*, Cambridge University Press: New York, 2006.
[32] J. Zhang, L. Zhang and W. Xu, "Surface plasmon polaritons: physics and applications," *Journal of Physics D: Applied Physics*, vol.45, pp. 113001-113020, 2012.
[33] M. Fukui, et al., "Lifetimes of surface plasmons in thin silver films," *Physica Status Solidi B*, vol. 91, pp. k61-k64, 1979.
[34] B. Prade, et al., "Guided optical waves in planner heterostructures with negative dielectric constant," *Physical Review B*, vol. 44, pp. 556-572, 1991.
[35] G. Mie, "Betlräge zur optic trüber medien, speziell kolloidaler metallösungen," *Annalen der Physik*, vol. 25, pp. 377-445, 1908.
[36] C. F. Bohren and D. R. Huffman, *Absorption and scattering of light by small particles*, Wiley: New York, 1983.
[37] S. A. Maier, *Plasmonics: Fundamentals and applications*, Springer: New York, Science and Business Media LLC, 2007.
[38] J. Du, et al., "Colorimetric chemodosimeter based on diazonium-gold-nanoparticle complexes for sulfite ion detection in solution," *Small*, 2012 (online published).

[39] N. J. Halas, et al., "Plasmons in strongly coupled metallic nanostructures," *Chemical Reviews,* vol. 111, pp. 3913-3961, 2011.
[40] M. Zavelani-Rossi, et al., "Near-field second-harmonic generation in single gold nanoparticles," *Applied Physics Letters,* vol. 92, pp. 093119-093123, 2008.
[41] C. Hubert, et al., "Role of surface plasmon in second harmonic generation from gold nanorods," *Applied Physics Letters,* vol. 90, pp. 181105-181108, 2007.
[42] J. E. Sipe, et al., "Analysis of second-harmonic generation at metal surfaces," *Physical Review B,* vol. 21, pp. 4389-4402, 1980.
[43] R. W. Boyd, *Nonlinear optics*, 3rd edition, Elsevier: New York, 2008.
[44] M. Pelton, et al. "Ultrafast resonant optical scattering from single gold nanorods: Large nonlinearities and plasmon saturation," *Physical Review B,* vol. 73, pp. 155419-155424, 2006.
[45] T. Utikal, et al., "Towards the origin of the nonlinear response in hybrid plasmonic systems," *Physical Review Letters,* vol. 106, pp. 133901-133904, 2011.
[46] M. Hentschel, et al., "Quantitative modeling of the third harmonic emission spectrum of plasmonic nanoantennas," *Nano Letters,* vol. 12, pp. 3778-3782, 2012.
[47] R. Jin, et al., "Photoinduced conversion of silver nanospheres to nanoprisms," *Science,* vol. 294, pp. 1901-1903, 2001.
[48] J. E. Millstone, et al., "Colloidal gold and silver triangular nanoprisms," *Small,* vol. 5, pp. 646-664, 2009.
[49] S. Chen, et al., "Synthesis and characterization of truncated triangular silver nanoplates," *Nano Letters,* vol. 2, pp. 1003-1007, 2002.
[50] D. Aherne, et al., "Optical properties and growth aspects of silver nanoprisms produced by a highly reproducible and rapid synthesis at room temperature," *Advanced Functional Materials*, vol. 18, pp. 2005-2018, 2008.
[51] G. S. Métraux and C. A. Mirkin, "Rapid thermal synthesis of silver nanoprisms with chemically tailorable thickness," *Advanced Materials,* vol. 17, pp. 412-415, 2005.
[52] H. Murayama, et al., "Ag triangular nanoplates synthesized by photo-induced reduction: Structure analysis and stability," *Chemical Physics Letters,* vol. 482, pp. 291-295, 2009.
[53] NCMN Electron Microscopy, (accessed Oct 20 2012), http://ncmn.unl.edu/cfem/microscopy/SEM.shtml.
[54] Electron Microbeam Analysis Laboratory, Michigan's Materials Characterization Facility, http://www.emal.engin.umich.edu/courses/SEM_lectureCW/SEM_Interaction.html.
[55] Universal Streak Camera C5680 Series, Hamamatsu Photonics, (accessed Oct 20 2012), http://sales.hamamatsu.com/assets/pdf/parts_C/e_C5680.pdf.
[56] Guide to streak cameras, Hamamatsu Photonics, (accessed Oct 20 2012), http://sales.hamamatsu.com/assets/pdf/hpspdf/Guidetostreak.pdf.
[57] High Performance Digital Temporal Analyser, (accessed Oct 20 2012), http://www.bilrc.caltech.edu/files/filecabinet/folder5/StreakCamera_text.pdf.
[58] Control & Readout System for Streak Cameras, (accessed Oct 20 2012), http://sales.hamamatsu.com/assets/pdf/hpspdf/HPD-TA.pdf.
[59] MicroChem Data Sheet, (accessed Oct 20 2012). http://microchem.com/pdf/PMMA_Data_Sheet.pdf.

[60] C. T. Yuan, et al., "Antibunching single-photon emission and blinking suppression of CdSe/ZnS quantum dots," *ACS Nano*, vol. 3, pp. 3051-3056, 2009.
[61] P. B. Johnson and R. W. Christy, "Optical-constants of noble-metals," *Physical Review B*, vol. 6, pp. 4370-4379, 1972.
[62] E. D. Palik, *Handbook of Optical Constants of Solids*, Academic Press: 1997.
[63] A. Lesuffleur, et al., "Enhanced second harmonic generation from nanoscale double-hole arrays in a gold film," *Applied Physics Letters*, vol. 88, pp. 261104-261106, 2006.
[64] A. Lesuffleur, et al., "Apex-enhanced second-harmonic generation by using double-hole arrays in a gold film," *Physical Review B*, vol. 75, pp. 045423-045427, 2007.
[65] F. Eftekhari and R. Gordon, "Enhanced second harmonic generation form noncentrosymmetric nanohole arrays in a gold film," *IEEE Journal of Selected Topics in Quantum Electronics*, vol. 14, pp. 1552-1558, 2008.
[66] D. Wang, et al., "High directivity optical antenna substrates for surface enhanced Raman scattering," *Advanced Materials*, vol. 24, pp. 4376-4380, 2012.
[67] A. Ahmed and R. Gordon, "Directivity enhanced Raman spectroscopy using nanoantennas," *Nano Letters*, vol. 11, pp. 1800-1803, 2011.
[68] Q. Min, Y. et al., "Substrate-based platform for boosting the surface-enhanced Raman of plasmonic nanoparticles," *Optics Express*, vol. 19, pp. 1648-1655, 2011.
[69] H. M. Miyazaki and Y. Kurokawa, "Squeezing visible light waves into a 3-nm-thick and 55-nm-long plasmon cavity," *Physical Review Letters*, vol. 96, pp. 097401, 2006.
[70] T. Søndergaard and S. I. Bozhevolnyi, "Strip and gap plasmon polariton optical resonators," *Physica Status Solidi B*, vol. 245, pp. 9-19. 2008.
[71] J. Jung, et al., "Gap plasmon-polariton nanoresonators: Scattering enhancement and launching of surface plasmon polaritons," *Physical Review B*, vol. 79, pp. 035401-035409, 2009.
[72] S. Kim, et al., "High-harmonic generation by resonant plasmon field enhancement," *Nature*, vol. 453, pp. 757-760, 2008.
[73] J. Butet,et al., "Sensing with multipolar second harmonic generation from spherical metallic nanoparticles," *Nano Letters*, vol. 12, pp. 1697-1701, 2012.
[74] Sigma-Aldrich, (accessed Oct 20 2012), http://www.sigmaaldrich.com/catalog/product/aldrich/698539?lang=en&region=CA.